Journal of Geochemical Exploration 183 (2017) 58–78

Contents lists available at ScienceDirect

Journal of Geochemical Exploration

journal homepage: www.elsevier.com/locate/gexplo

Geochemistry, geochronology, isotope and fluid inclusion studies of the Kuh-e-Zar deposit, Khaf-Kashmar-Bardaskan magmatic belt, NE Iran: Evidence of gold-rich iron oxide–copper–gold deposit

Mohammad Hassan Karimpour[a,*], Azadeh Malekzadeh Shafaroudi[a], Alireza Mazloumi Bajestani[b], Richard Keith Schader[c], Charles R. Stern[c], Lang Farmer[c], Martiya Sadeghi[d]

[a] Research Center for Ore Deposit of Eastern Iran, Ferdowsi University of Mashhad, P.O. Box 91775-1436, Mashhad, Iran
[b] Department of Geology, Payam-e Noor University, Mashhad, Iran
[c] Department of Geological Sciences, University of Colorado, CB-399, Boulder, CO 80309-399, USA
[d] Department of Mineral Resources, Geological Survey of Sweden, Uppsala, Sweden

ARTICLE INFO

Keywords:
Iron oxide-copper-gold deposit
Petrogenesis
Fluid inclusion
Kuh-e-Zar
Khaf-Kashmar-Bardaskan magmatic belt
NE Iran

ABSTRACT

The Kuh-e-Zar deposit is located in the central part of the Khaf-Kashmar-Bardaskan Tertiary magmatic belt, NE Iran. The prevailing stratigraphic unit is composed of Cenozoic volcanic rocks (rhyolitic to andesitic in composition), which are intruded by subvolcanic plutons. Intrusive rocks spatially close to mineralization include metaluminous to peraluminous, calc-alkaline and I-type diorite, granodiorite, quartz monzonite, quartz monzodiorite, and syenogranite. The quartz monzonite and quartz monzodiorite have identical zircon U–Pb ages of ca. 40.7–41.2 Ma. The intrusions are characterized by enrichment in large-ion-lithophile elements (LILEs) and light rare-earth-elements (LREEs), depletion in heavy rare-earth-elements (REEs, $La_N/Yb_N \approx 7$ to 9.07) and high-field-strength-elements (HFSEs) and εNd(t) ranging from −0.06 to −2.93 at $^{86}Sr/^{87}Sr(t) = 0.7054–0.7064$ and $^{206}Pb/^{204}Pbi = 18.6–18.71$. The intrusive rocks of Kuh-e-Zar are products of crustal assimilation by melts derived from the metasomatized mantle wedge above the subducting Neotethyan Ocean slab beneath SW Eurasia.

Field work and mineralogical, petrological studies show that, the hydrothermal alteration produced a zone of silicification, propylitic alteration, and albitization associated with minor sericitic-argillic alteration. The mineralization of Kuh-e-Zar occurs in veins, stockworks, and breccias, which is located near or within NE − SW and NW − SE faults cutting through volcanic rocks and wall rocks. The ore minerals are dominated by specular hematite and gold with small amounts of pyrite, chalcopyrite, and galena. Hematite, goethite, malachite, covellite, and cerussite are secondary minerals. The main gangue minerals include quartz, siderite, chlorite, and albite. Microthermometric study of fluid inclusions shows homogenization temperatures at medium-high temperature of 248 to 491 °C. Salinities of ore-forming fluids are medium-low ranged from 4 to 19.2 wt% NaCl equivalent. The sulfur isotope composition of chalcopyrite ($\delta^{34}S = -2.5$ to 0.9‰) suggests that sulfur was derived mainly from igneous rocks. The oxygen isotopic data ($\delta^{18}O_{water} = 7.4–7.9‰$) indicate that the ore fluids were in magmatic origin.

The mineralogy, alteration, geochemistry, stable isotopes, and petrogenesis of intrusions of the Kuh-e-Zar deposit indicate it is an Eocene gold-rich iron oxide-copper-gold (IOCG) deposit.

1. Introduction

The geological settings, hydrothermal alteration and mineralizing fluid compositions vary between deposits of the "IOCG-type" (Hitzman et al., 1992; Sillitoe, 2003). However, they are a class of Cu ± Au deposits containing abundant low-Ti iron oxide (magnetite and/or hematite) and extensive hydrothermal alkali (Na/Ca/K) alteration. Such deposits also show strong structural controls, and a temporal but not a close spatial association with igneous rocks (Williams et al., 2005). They formed in rift or subduction settings (Hitzman, 2000; Barton, 2014) from the Late Archean to Pliocene (Groves et al., 2010). Available data suggest that IOCG deposits formed from

* Corresponding author.
E-mail addresses: karimpur@um.ac.ir (M.H. Karimpour), shafaroudi@um.ac.ir (A. Malekzadeh Shafaroudi), Richard.Schader@colorado.edu (R.K. Schader), charles.stern@colorado.edu (C.R. Stern), farmer@cires.colorado.edu (L. Farmer), martiya.sadeghi@sgu.se (M. Sadeghi).

http://dx.doi.org/10.1016/j.gexplo.2017.10.001
Received 31 January 2017; Received in revised form 4 September 2017; Accepted 1 October 2017
Available online 03 October 2017
0375-6742/

magmatic–hydrothermal systems where the ore-forming fluids were at moderate temperature (~300–450 °C), and had high salinity and CO_2 (e.g. Pollard, 2001, 2006; Fu et al., 2003; Rieger et al., 2012). However, many IOCG deposits, particularly during the Cu-Au mineralization stage, are characterized by high-salinity fluids with variable CO_2 content and medium-to-low temperature (< 300 °C). According to Williams (2010), IOCG deposits formed in a variety of hydrological systems, including high-level systems, in which cool surficial fluids interacted with deep sourced magmatic fluids. Although there is good evidence for the genesis of IOCG deposits, there is a controversy on the nature of ore-forming fluids responsible for Cu-Au mineralization and their relationship with IOCG deposits during the preceding magnetite mineralization (Chen et al., 2011).

The Khaf-Kashmar-Bardaskan magmatic belt (KKBMB), located in northeastern Iran, is one of the most important metallogenic province in Iran that comprises numerous porphyry Au-Cu and Cu deposits, iron-oxide copper-gold (IOCG) deposits, skarn Fe deposits, vein-type Cu-Au and Au-Ag deposits, stratabound Cu deposits, and kaolin deposits (Karimpour, 2006; Karimpour and Malekzadeh Shafaroudi, 2006; Saadat et al., 2007; Yousefi et al., 2009; Golmohammadi et al., 2015; Almasi et al., 2015; Mahvashi and Malekzadeh Shafaroudi, 2016) (Fig. 1a and b). Karimpour (2004) suggested the KKBMB has good potential for IOCG-type mineralization in NE Iran.

The Kuh-e-Zar deposit is located in the center of the KKBMB, approximately 40 km NW of the town called Torbat (Fig. 1b). Having a proven reserve of over 3 Mt gold ore @ 3 ppm Au, and with low concentrations of As, the Kuh-e-Zar represents a unique gold deposit in Iran. The gold mineralization consists of fifteen blocks defined in the mine. Modern mining activity only started after 1997. Extensive exploration began in 1999.

Previous studies were mainly limited to the exploration reports of Zarmehr Company (1999a,b, 2000, 2002, 2005a,b), MS.C. thesis (Shahbazian, 2000; Gurabjiripour, 2001; Shirzad, 2002; Ansari Jafari, 2014), and Iranian journal papers (Karimpour and Mazloumi Bajestani, 1999; Abedi, 2003; Mazloumi Bajestani et al., 2007; Mazloumi Bajestani and Rasa, 2010). The geology of deposit, structural analysis, and minor geochemistry of intrusions and orebodies that create them (Karimpour and Mazloumi Bajestani, 1999; Abedi, 2003; Mazloumi Bajestani et al., 2007; Mazloumi Bajestani and Rasa, 2010) had been relatively well studied. In contrast, paragenetic assemblages of alteration and mineralization, age and petrogenesis of intrusive rocks and their relationship to mineralization, and nature of ore-fluid have not been investigated in detail yet. Yaghoubpour et al. (1999) and Shahbazian (2000) suggested that the Kuh-e-Zar deposit is a low sulfide epithermal Au deposit, whereas many features of the Kuh-e-Zar deposit are typical of IOCG deposits that are now widely recognized as a global class of ore deposits (e.g., Hitzman et al., 1992; Barton and Johnson, 1996; Hitzman, 2000; Sillitoe, 2003; Groves et al., 2010).

This paper is based on field works over two decades that focused on the geologic-alteration mapping, recognition of different mineralized zones and mineral paragenesis, intrusive bodies and their relationship to mineralization, their geochronology and petrogenesis, and the mineralogy, fluid inclusion, and stable isotope studies of the deposit. The primary outcome of this study was the recognition of the Kuh-e-Zar deposit as an iron oxide-copper-gold (IOCG) deposit with enrichment of Au and depletion of Cu.

2. Geological background

Cenozoic igneous rocks in Iran are distributed in five belts (Fig. 1a) including the KKBMB in northeastern Iran. The KKBMB is an arcuate, W-E to NW-SE trending, Cenozoic volcano-plutonic arc of 400 km in length and 50 km in width, which located in the north of the major Doruneh Fault (Fig. 1a and b). This belt has significant potential for iron, copper, gold, and silver deposits (Karimpour, 2004; Yousefi et al., 2009; Malekzadeh Shafaroudi et al., 2013; Golmohammadi et al., 2015) (Fig. 1b). The regional tectonomorphology are resulted from the Alpidic orogenesis, whereas the main lineaments and the general strike of the mountain ranges reflect reactivation of earlier Assyntic orogenic structures (Eftekharnejad, 1981).The two blocks of Sabzevar in the north and Lut in the south of the Doruneh Fault show dextral and sinistral movements in different periods respectively, with the dextral movement being the most recent (Aghanabati, 2004). The structural features of the region, such as faults and foldings, as well as the strike of the formations, follow the NW-SE to NE-SW direction of the major Doruneh Fault (Fig. 1b). A series of NW-SE and NE-SW striking faults (N140) with sinistral and dextral movements have played a role in the formation of the Khu-e-Zar orebodies.

The major rock types in the Kuh-e-Zar deposit are Cenozoic calc-alkaline volcanic rocks and subvolcanic intrusive stocks and dikes intruded into volcanic rocks (Fig. 2). The volcanic rocks mainly consist of Paleocene to middle Eocene rhyolitic-dacitic pyroclastic rocks, rhyolitic lapilli tuff, quartz latite, trachyt, hornblende quartz latite, and trachyandesite and minor rhyolitic welded tuff and ignimbrite, and andesitic agglomerate. These volcanic rocks are intensely altered, especially in the vicinity of the mineralized zones in the southeastern part of the area, and they are the primary hosts of gold ± copper mineralization veins in the Kuh-e-Zar deposit. Pleistocene-Quaternary pyroxene andesite and basalt also occur in the area (Fig. 2).

The plutonic and subvolcanic intrusive rocks, which are exposed as stocks and dikes in the northern, northeastern, and southwestern parts of the area, consist of six compositional groups, which include 1) hornblende-pyroxene diorite porphyry; 2) hornblende-biotite granodiorite; 3) biotite-hornblende quartz monzonite porphyry; 4) biotite-hornblende quartz monzodiorite porphyry; 5) syenogranite; and 6) hornblende quartz monzonite porphyry (Figs. 2 and 3a to h). The ~40 Ma zircon U-Pb ages obtained from the quartz monzodiorite and quartz monzonite indicate a Middle Eocene intrusion (see Section 7.2). These acidic to intermediate intrusions have spatial relationship to mineralization and they are host rock in a few places (Fig. 3i), but temporal relationship is unclear. However, we could to suggest the intrusions with the same composition and age in depth probably led to the development of a variety of alteration and formation of mineralized zones in their host volcanic rocks in the area.

3. Petrography of the plutonic and subvolcanic intrusions

Hornblende-pyroxene diorite porphyry occurs as two small outcrops in the western part of the Kuh-e-Zar deposit (Fig. 2). Hornblende-pyroxene diorite porphyry consists of ~40% phenocrysts, including 20–25% plagioclase, 8–10% augite, and 3–5% hornblende in a fine-grained groundmass (Fig. 4a). Magnetite is common accessory mineral. The diorite is weakly to moderately altered, with chlorite being a common alteration mineral.

Biotite-hornblende quartz monzodiorite porphyry is one of the most widely exposed intrusive rocks in the study area (Figs. 2 and 3e). The biotite-hornblende quartz monzodiorite porphyry has porphyritic, glomeroporphyritic, and granophyric texture with medium-grained groundmass and normally contains up to 50% phenocrysts, including 20–25% plagioclase, 5–8% K-feldspar, 4–6% hornblende, 5–8% quartz, and 2–3% biotite. The same minerals are also present in the groundmass (Fig. 4b). Accessory minerals are magnetite, zircon, and apatite. Hornblende and biotite are replaced by chlorite in some places. A small amount of feldspar phenocrysts have been altered to sericite and albite. Minor secondary quartz also exists in the groundmass.

Biotite-hornblende quartz monzonite porphyry crops out as stocks in the western to southwestern part of the Kuh-e-Zar deposit (Figs. 2 and 3c). The biotite-hornblende quartz monzonite porphyry has a porphyritic and glomeroporphyritic texture with fine-grained groundmass. The phenocrysts consist of 10–12% plagioclase, 15–20% K-feldspar, 5–8% quartz, 2–3% hornblende, and 1–2% biotite (Fig. 4c). Magnetite and zircon are accessory minerals. Sericite is the main

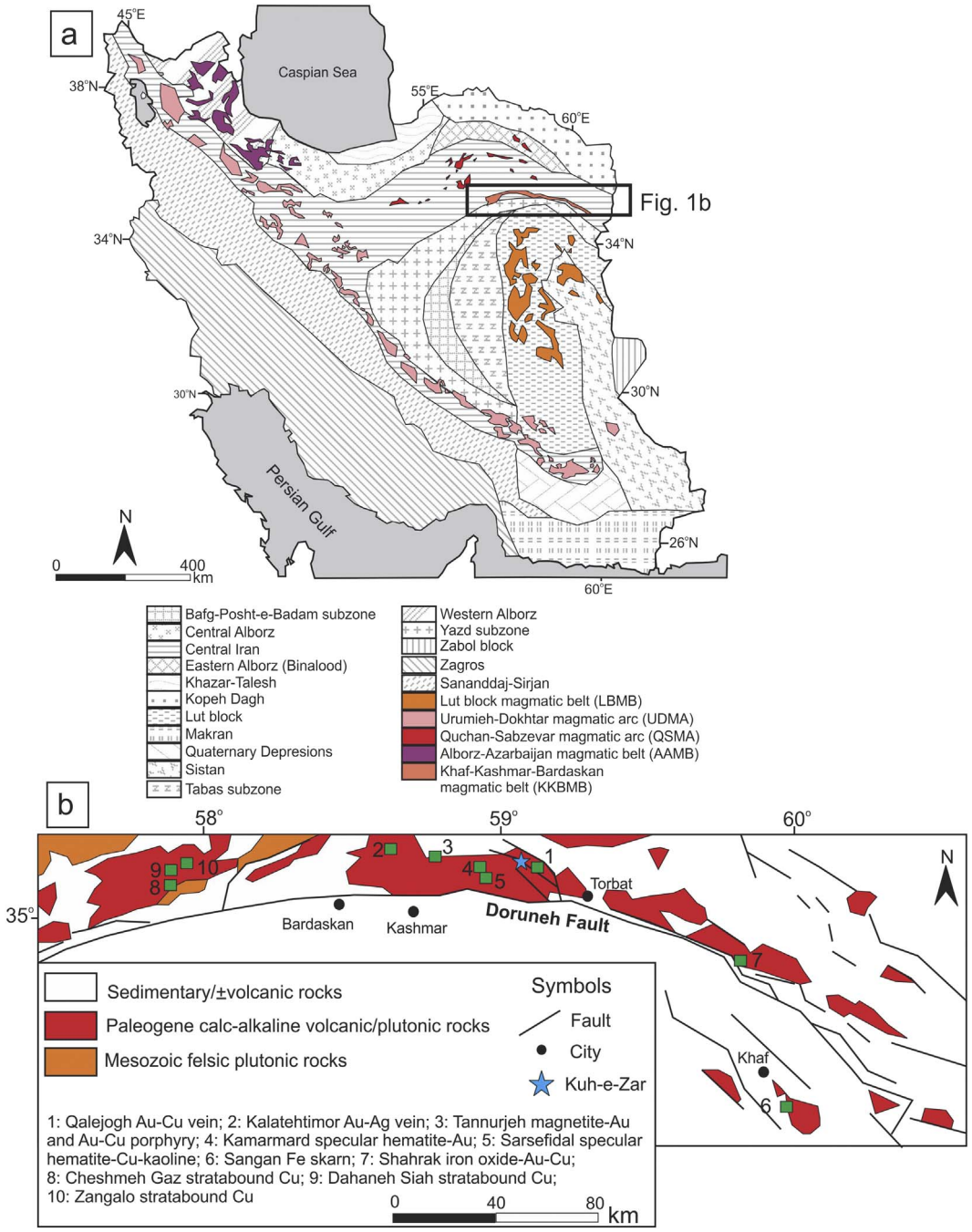

Fig. 1. a) Geological-structural map of Iran (modified from Sahandi et al., 2002), b) simplified geological map of Khaf-Kashmar-Bardaskan magmatic belt (KKBMB) and the location of Kuh-e-Zar iron oxide-gold deposit and other known ore deposits.

secondary mineral in some places. Feldspar and mafic minerals have been altered to sericite and chlorite, respectively.

Hornblende-biotite granodiorite is exposed in three locations in the central part of Kuh-e-Zar deposit (Figs. 2 and 3a). The hornblende-biotite granodiorite has granular texture and consists of 25–30% quartz, 30–35% plagioclase, 15–18% K-feldspar, 5–10% biotite, and 5–8% hornblende (Fig. 4d). Accessory minerals are magnetite, zircon, and apatite. The hornblende and biotite are replaced by chlorite and feldspars are altered to albite and sericite.

Syenogranite, which is one the most widely exposed intrusions in the area (Figs. 2 and 3g), has granular and granophyric textures. The syenogranite normally contains up to 40% quartz, 40–45% K-feldspar, and 8–15% plagioclase. The same minerals are also present in the groundmass (Fig. 4e). Accessory minerals include magnetite and zircon. The feldspars are altered to albite and minor sericite and clay minerals. The intensity of alteration increases in the vicinity of mineralization veins.

Hornblende quartz monzonite porphyry occurs as three small dikes in the eastern part of the Kuh-e-Zar deposit. This unit crosscuts the hornblende-biotite granodiorite unit and is the youngest intrusive rock in the area (Fig. 2). It contains phenocrysts that consist of 10–12% plagioclase, 10–15% K-feldspar, and 5–8% quartz (Fig. 4f). Magnetite is an accessory mineral. The hornblende quartz monzonite porphyry is unmineralized, but has undergone pervasive propylitic alteration, where hornblende phenocrysts are altered to chlorite and epidote veinlets are observed in some places.

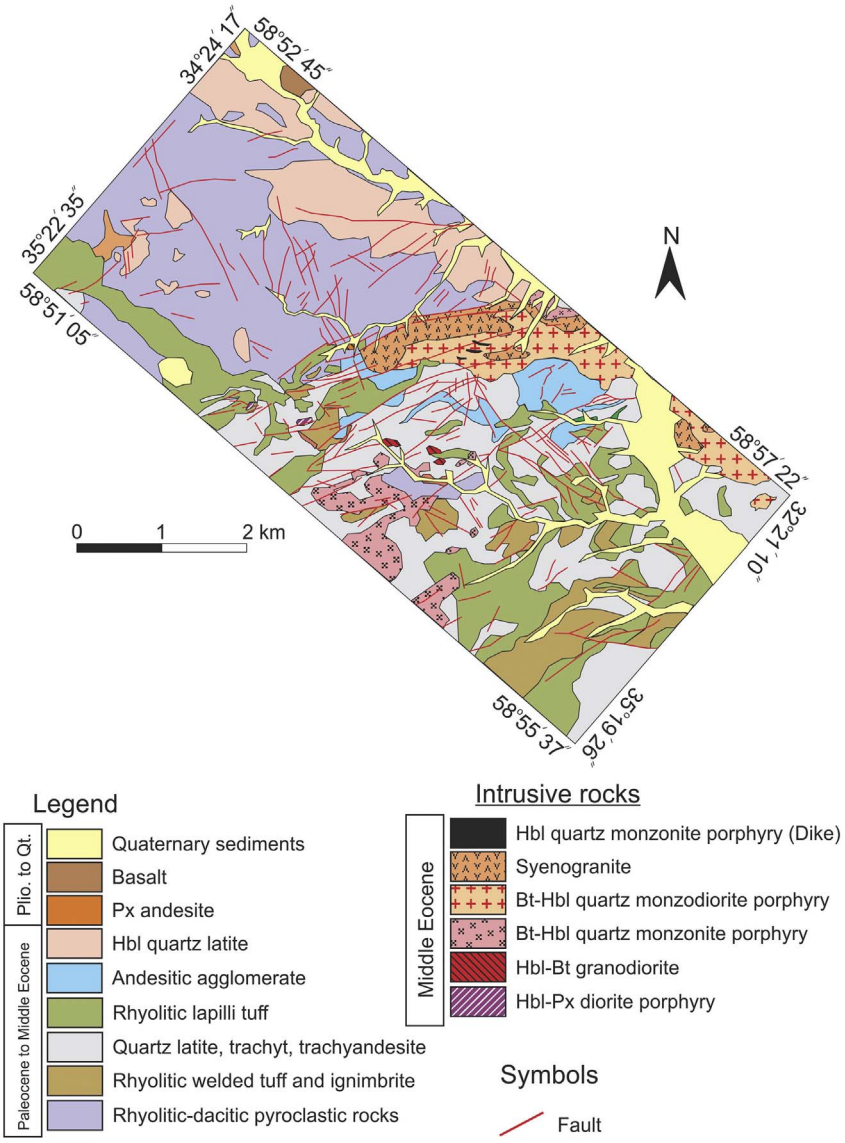

Fig. 2. Geologic map of the Kuh-e-Zar deposit (modified after Zarmehr Company, 2005b) (Hbl: hornblende, Bt: biotite, Px: pyroxene (Whitney and Evans, 2010)).

4. Mineralization and hydrothermal alteration

Mineralization at Kuh-e-Zar deposit occurs mainly within the volcanic rocks (rhyolitic-dacitic pyroclastic rocks, rhyolitic tuff, and latitic-trachytic lava) and comprises several orebodies with similar alteration, mineralogy and texture. The orebodies are composed of fifteen individual major iron oxide–gold veins together and several minor veins (Table 1), which extend in the N60°E and N20°–35°W directions, filling fractures and faults of the same trend along parallel fault zones (Fig. 5). These fractures were produced by tensile stresses and functioned as channel ways for the ore bearing solutions. The iron oxide–gold veins range from 1 to 30 m in width, from 60 to 2800 m in length, and dip 70–90° south (Table 1). The mineralization is characterized by brecciate, stockwork-like, and open space filling textures (Fig. 6a to e). Stockwork-like texture, filling fractures of host rock, is a common texture of the deposit. The veinlets vary in thickness from a few millimeters to 10 cm (Fig. 6c and d). The veinlets generally consist of specular hematite, quartz, gold, and siderite. Brecciated iron oxide ore is the second most dominant texture at the deposit. It consists of altered angular brecciated fragments of the host rock cemented by specular hematite, quartz, and gold, which are similar to hydrothermal breccia (Fig. 6e).

The ore minerals at the Kuh-e-Zar deposit are dominated by specular hematite and gold with small amounts of pyrite, chalcopyrite, and galena. Hematite, goethite, malachite, covellite, and cerussite are secondary minerals that developed from the primary ones through weathering (Table 1). The main gangue minerals include quartz, siderite, chlorite, and albite (Fig. 7). Specular hematite is commonly bladed-shape and varies in size from a few millimeters to up to 1 cm (Fig. 8a to d). This mineral Gold is the main Au-bearing mineral, and is observed between blades of specular hematite and quartz crystals. The size of the gold particles varies from 1 to 185 μm; 1 to 10 μm is the most common size with a mean of 8.52 μm (Fig. 8a to d and Table 1). Minor pyrite, chalcopyrite, and galena as main sulfide minerals mostly occur in the mineralized zones within intrusive rocks. Pyrite presents as euhedral and/or subhedral small grains (up to 0.2 mm) disseminated in veins among other minerals (Fig. 8e). This mineral is partly or wholly transformed into goethite. Chalcopyrite is found as small to medium grains (0.1 to 0.6 mm) in malachite, hematite, goethite, and covellite and occurs as relicts (Fig. 8f and g). Galena occurs as single grains in quartz veinlet and a few crystals are up to 0.8 mm in size (Fig. 8h). Cerussite is observed as mostly overgrowths along the borders, cracks, and cleavages of galena. Covellite occurs at contacts between galena and gangue minerals (Fig. 8h). The generalized paragenetic sequence is divided into two main stages (Fig. 7): (1) hypogene stage of chlorite, silica, siderite, and albite alteration associated with specular hematite,

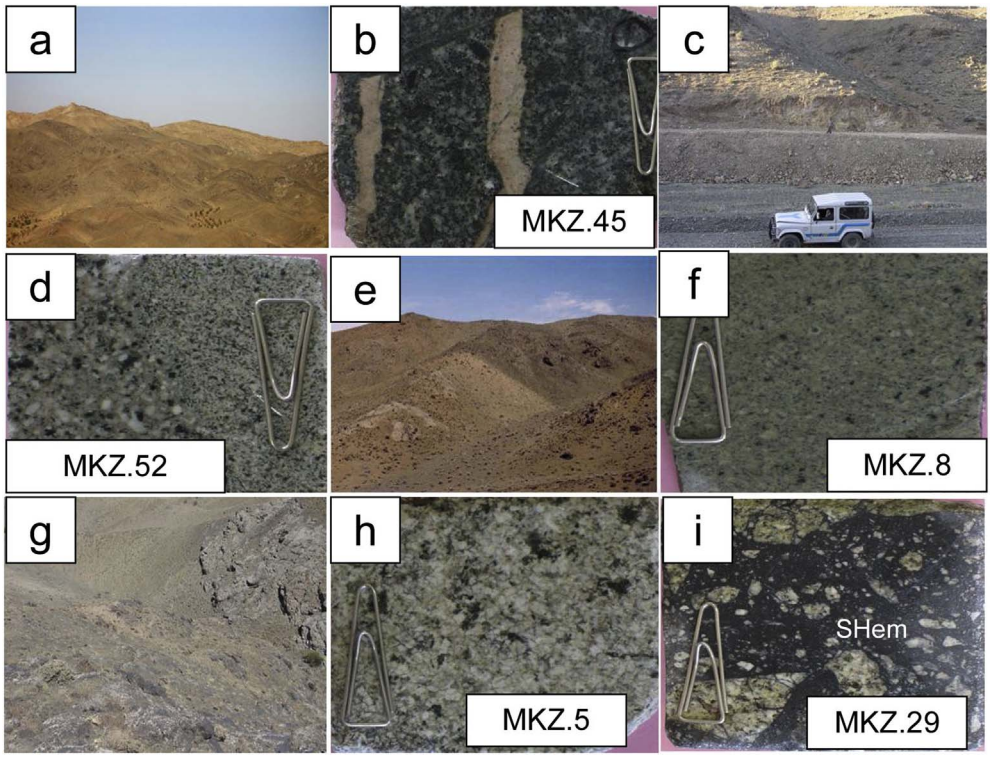

Fig. 3. Outcrop and hand specimen photos of a. Hbl-Bt granodiorite, b. Hbl-Bt granodiorite, which cut by aplitic vein, c. Bt-Hbl quartz monzonite porphyry, d. Bt-Hbl quartz monzonite porphyry in hand specimen, e. Bt-Hbl quartz monzodiorite porphyry, f. Bt-Hbl quartz monzodiorite porphyry in hand specimen, g. syenogranite, h. syenogranite in hand specimen, i: brecciated syenogranite that they are cemented by specular hematite and minor hydrothermal quartz (Hbl: hornblende, Bt: biotite, SHem: specular hematite (Whitney and Evans, 2010)).

gold, chalcopyrite, pyrite, and galena (2) hematite, goethite, malachite, covellite, and cerussite formation at oxidized zone. Generation of abundant chlorite seems to be the first stage of mineralization. Massive specular hematite forms the cement of chloritized breccias at the Kuh-e-Zar (Fig. 6e). Open space filling texture is mostly characterized by specular hematite at margin and quartz in center of veinlet (Fig. 6c), which show quartz deposited after specular hematite, whereas siderite occurs at margin of a few veinlets in open space filling texture and forms earlier than specular hematite (Fig. 6d). Most of siderite mineral occurs at late stage of hypogene mineralization and cuts other minerals. Gold is observed between blades of specular hematite and quartz crystals and seems to be synchronized to them. Chlorite alteration is overprinted by albite. Chalcopyrite overgrows specular hematite needles, whereas there is no clear relationship between pyrite and galena with other ore minerals (Fig. 7). In general, mineral assemblages of Kuh-e-Zar deposit can be simplified in three different veins, including 1) quartz–specular hematite–gold, 2) quartz–specular hematite–-gold ± pyrite ± chalcopyrite, and 3) quartz–specular hematite–-gold ± siderite. Field and laboratory observations indicate most of quartz–specular hematite–gold veins have been cut off by

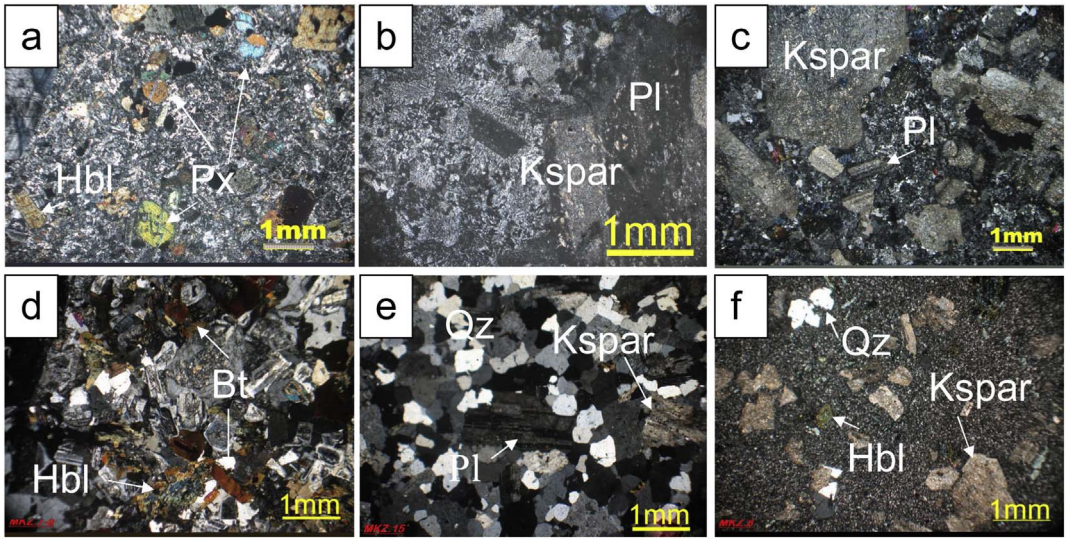

Fig. 4. Photomicrograph of a. Hornblende-pyroxene diorite porphyry with porphyry texture and fine-grained groundmass composed of plagioclase, hornblende, pyroxene, and opaque minerals. b. Biotite-hornblende quartz monzodiorite porphyry with glomeroporphyritic and granophyric textures. c. Biotite-hornblende quartz monzonite porphyry showing plagioclase, K-feldspar, and hornblende minerals. d. Hornblende-biotite granodiorite with medium-grained hypidiomorphic granular texture affected by propylitic alteration. e. syenogranite with medium-grained hypidiomorphic granular texture showing quartz, K-feldspar, and plagioclase minerals. f. Hornblende quartz monzonite porphyry with porphyry texture showing K-feldspar, hornblende, and quartz minerals. (All photos in cross-polarized light; Qz = quartz, Hbl: hornblende, Bt: biotite, Px: pyroxene, Kspar: K-feldspar, and Pl: plagioclase (Whitney and Evans, 2010).)

Table 1
Summarized description of fifteen individual major veins from the Kuh-e-Zar area.

Mineralized zone	Host rock	Strike & dip	Thickness (m)	Length (m)	Mineralogy[a]	Alteration[b]	Size of gold grain (μm)	Grade
Shahriar	Rhyolitic lapilli tuff	Strike: N43°W Dip: 65–80°SW	3 to 8	Up to 400	SHem (10–50%), Qz (50–95%), Au, Py (< 1%), Sd (1–3%)	Si, Pr	3 to 20, average 5.8	Au = 0.16–6 ppm, Cu < 178 ppm, Ag < 8 ppm, Zn < 615 ppm, Pb < 248
Alireza	Rhyolitic lapilli tuff and latitic, trachytic, trachyandesitic lavas	Strike: N5°W to N35°W Dip: 84°S	0.5 to 3	Up to 400	SHem (10–40%), Qz (60–90%), Au, minor Py, Sd, Ccp	Si, Pr	3 to 107	Au = 0.58–6.8 ppm, Cu < 189 ppm, Ag < 12 ppm, Zn < 219 ppm, Pb < 361 ppm
Gholleh Khord	Andesitic agglomerate	Strike: N65°E Dip: 75°SE	1 to 2	300	SHem (15–30%), Qz (70–95%), Au	Si, Pr, Ser	Average 6.2	Au = 3.8 ppm
Ghar-e-Saleh	Rhyolitic lapilli tuff, basalt, latite, trachyandesite	Strike: N49°–67°E	1 to 30	795	SHem (15–40%), Qz (50–80%), Au, Sd (2–3%), Py, Ccp (1–2%)	Si, Pr, Ser. Ar	10 to 83 average 27	Au = 0.6–12.6 ppm, Cu = 64 ppm–1.3%, Ag ≤ 1–273 ppm, Zn < 0.5%, Pb < 1%
Tarik Darreh	Latite, trachyt, trachyandesite	Strike: N30°E to N70°E Dip: 77°–82°SE	3 to 5	385 to 520	Qz, SHem (5–10%), Au, Py, Ccp, Gn	Si	Average 18.2	Au = 0.2–6.7 ppm, Cu = 351 ppm to 2%, Ag < 7 ppm, Zn < 624 ppm, Pb < 102 ppm
Shah Ali	Latite, trachyt, trachyandesite	Strike: N15°E Dip: 80°SE	0.3 to 1.2	Up to 1000	SHem (15–30%), Qz (70–90%), Au	Si, Pr	3 to 93 average 12.5	Au = up to 34 ppm
Bazeh Moushi	Rhyolitic lapilli tuff, latite, and trachyandesite	Strike: N62°–67°E	1 to 15	630	SHem (15–40%), Qz (60–90%), Au, Sd (1–2%), Ccp, Py, Gn	Si, Pr	14.2	Au ≤ 2 ppm, Cu < 0.6%
Amrollahi	Pyroclastic rocks acid-intermediate lavas	Strike: N35°–76°E Dip: 84°SE	0.5 to 4	Up to 400	SHem (5–30%), Qz (70–95%), Au, Sd (1–5%), Py, Gn	Si, Pr, Ser	3 to 20, one grain 185	Au = 2.5 ppm
Khosh Bazeh	Rhyolitic lapilli tuff, andesitic agglomerate, latite, trachyandesite	Strike: N20°–60°E	0.7 to 10	Up to 60	Sd (up to 50%), SHem(5–50%), Qz (50–95%), Au, Py, Ccp	Si, Pr	3 to 45 average 7.1	Au = 3.2 ppm
Kamar Zard	Rhyolitic-dacitic pyroclastic rocks, hornblende quartz latite	Strike: N27°–32°E to N10°E	–	–	Gth (40–50%), Qz (40–60%), Py (20–25%), Hem (2–5%), Ccp (2–5%), Gn (1–2%), Au, SHem	Si, Pr, Ar	5 to 55 average 25.7	Au = 8 ppm, Cu up to 5%, Ag < 9 ppm, Zn < 0.1%, Pb up to 2%
Ghar-e-Kaftari	Andesitic agglomerate	Strike: N15°–47°E	0.5 to 30	430	SHem (5–40%), Qz (30–80%), Au, Sd (1–5%), Ccp	Si, Pr, Ser	2 to 100 average 6.1	Au = 0.1–10 ppm, Cu < 0.8%, Ag < 10 ppm, Zn < 840 ppm, Pb < 300 ppm
Farshami	Latite, trachyt, trachyandesite, andesitic agglomerate	Strike: N65°E	0.6 to 8	400	SHem (5–30%), Qz (60–90%), Au, Ccp (1–10%), Py (> 1%)	Si, Pr	15 to 25	Au = 0.1–14 ppm, Cu < 1.3%, Ag < 33 ppm, Zn < 550 ppm, Pb < 700 ppm
Tangeh Piazi	Rhyolitic-dacitic pyroclastic rocks, rhyolitic tuff, andesitic agglomerate	Strike: N35°E Dip: 85°SE	1 to 5	1140	SHem (30–50%), Qz (60–90%), Au, Sd (2–3%), Py (> 2%)	Si, Pr	Generally > 5	Au = up to 36 ppm, Cu < 0.6%,
Mohammad Baigi	Rhyolitic-dacitic pyroclastic rocks, rhyolitic tuff, andesitic agglomerate, quartz monzodiorite porphyry, syenogranite	Strike: N67°–72°E Dip: 83°SE	0.9 to 20	Up to 2800	SHem (10–50%), Qz (40–95%), Au, Sd (3–5%), Py, Ccp, Gn	Si, Pr, Alb	3 to 170 average 9.74	Au = 0.2–9.6 ppm, Cu < 125 ppm–3.83%, Ag < 4 ppm, Zn < 740 ppm, Pb < 330 ppm
Hossein Abad	Rhyolitic-dacitic pyroclastic rocks, rhyolitic lapilli tuff	Strike: N55°E	2.5 to 12	400	SHem (10–20%), Qz (60–90%), Au, Sd, Py, Ccp, Gn	Si, Pr	3 to 120 average 25.8	Au = 0.1–5 ppm

[a] SHem: specular hematite, Qz: quartz, Sd: siderite, Au: gold, Py: pyrite, Ccp: chalcopyrite, Gn: Galena, Gth: goethite, Hem: hematite (Whitney and Evans, 2010).
[b] Si: silicification, Pr: propylitic, Ser: sericitic, Ar: argillic, Alb: albitization.

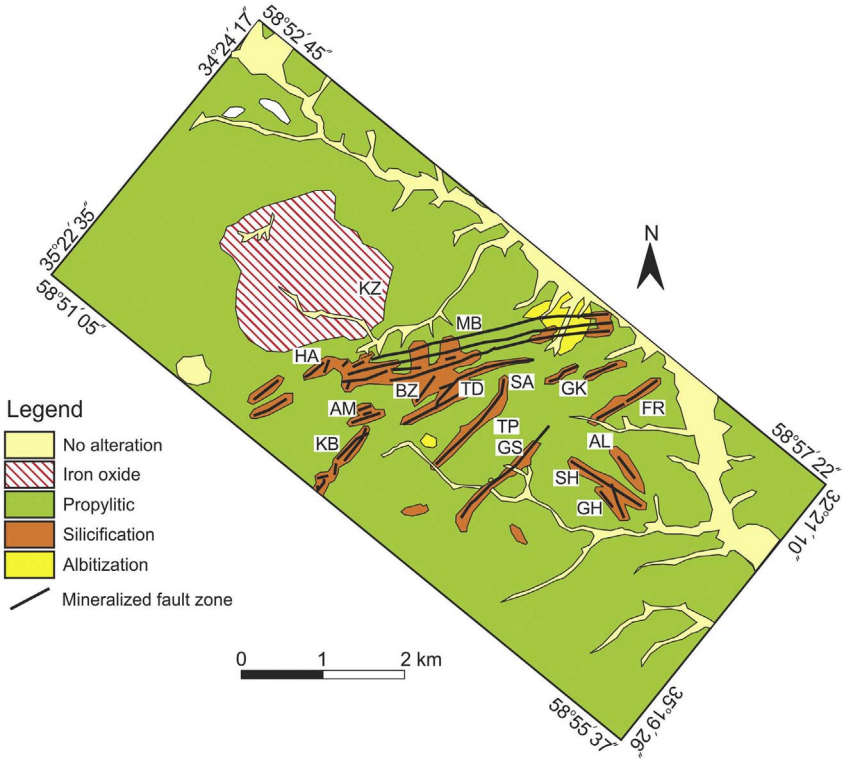

Fig. 5. Alteration map of the Kuh-e-Zar deposit and location of mineralized zones.

SH: Shahriar; AL: Alireza; GK: Gholleh Khord; GS: Ghar-e-Saleh; TD: Tarik Darreh; SA: Shah Ali; BZ: Bazeh Moushi; AM: Amrollahi; KB: Khosh Bazeh; KZ: Kamar Zard; GH: Ghar-e-Kaftari; FR: Farshami; TP: Tangeh Piazi; MB: Mohammad Baigi; HA: Hossein Abad;

quartz–specular hematite–gold ± pyrite ± chalcopyrite veins and these veins containing pyrite and chalcopyrite are younger. Also, siderite-bearing veins are mainly formed in later stage according to crosscutting relation because quartz–specular hematite–gold ± siderite veins mostly cut both quartz–specular hematite–gold and quartz–-specular hematite–gold ± pyrite ± chalcopyrite veins in the area.

Hydrothermal alteration has affected all exposed volcanic and intrusive rocks at Kuh-e-Zar within an area of 40 km^2. Hypogene alteration includes silicification, propylitic, and albitization zones; however, minor sericitic-argillic zones are observed within intrusive rocks (Fig. 5 and Table 1).

Silicification alteration, which is spatially associated with all the gold mineralized zones, occurs as distal alteration in both hanging wall and footwall host rocks (Fig. 5). The siliceous composition makes 15% to 60% of the rocks' volumes, forming fine-grained (<50 μm) to coarse-grained (> 1 mm) quartz aggregates (Fig. 9a to c). *Propylitic alteration* is very widespread (Fig. 5) and affects the volcanic and intrusive rocks. It consists of chlorite (<35%), epidote (<10%), calcite (<10%), and magnetite (<2%) with minor amounts of sericite. Mafic minerals and plagioclase were altered to chlorite, epidote, and calcite. Additionally, veinlets of quartz-epidote-chlorite, chlorite-epidote, epidote-quartz, quartz-calcite, calcite, chlorite-calcite, and epidote-calcite are observed (Fig. 9d to g). *Albitization alteration*, which is recognized in hornblende-biotite granodiorite, biotite-hornblende quartz monzodiorite porphyry, and syenogranite, is exposed in the center of the area (Fig. 5). Albite mainly occurs as replacements of plagioclase (andesine and oligoclase). The sodic composition makes ≤7% of the rock's volume (Fig. 9h). *Sericitic-argillic alteration* occurs mainly in intrusions. Feldspar (plagioclase and K-feldspar) was altered to sericite (< 30%) and clay minerals (< 10%). Minor quartz occurs as veinlets in this alteration zone (Fig. 9i).

5. Analytical methods

> 300 polished slabs and thin sections were prepared, from the mineralized zones and volcanic and intrusive rock from the Kuh-e-Zar deposit, for microscopic study. From intrusive rocks, thirteen samples were selected from the least altered samples for bulk rock analysis. Major elements were determined by wave-length dispersive X-ray fluorescence spectrometer using fused disks, and by a Phillips PW 1480 XRF spectrometer at the Ferdowsi University of Mashhad, Iran. A set of international and Iranian rock standards including MRG-1, MG-4, JG-2, JR-1, SY-2, SY-3, JSL-1, MK-1, NIM-S, and NCS-307, were used for calibration. Trace element and REE analysis was carried out at ACME Laboratory of Canada using ICP-MS techniques following lithium metaborate/tetraborate fusion after nitric acid digestion for 8 samples.

Two rock samples were selected from the intrusions for U-Pb zircon age dating, one from the quartz monzonite (sample MKZ-13) and another from the quartz monzodiorite (sample MKZ-7). Around 70 zircon grains were isolated from each rock sample by using standard mineral separation techniques at Ferdowsi University of Mashhad. U-Pb isotope data were collected using a New Wave 193 nm ArF laser ablation system coupled to a Nu Plasma HR inductively coupled plasma-mass spectrometer (ICP-MS) at the Arizona Laserchron Center using methods described by Gehrels et al. (2008).

Five rock samples (MKZ-7, MKZ-13, MKZ-20, MKZ-11, and FZ, 56) were selected from the least altered intrusions for Rb/Sr, Sm/Nd, and Pb isotope analysis. Sr, Nd, and Pb isotopic analyses were performed on a 6-collector Finnigan MAT 261 Thermal Ionization Mass Spectrometer at the University of Colorado, Boulder (USA) as described by Farmer et al. (2003).

Metal concentrations were carried out at N.F.C. Laboratory of China, BRGM laboratory of Feranch, and Muteh Gold Company laboratory of Iran using ICP-MS and atomic absorption techniques following hot Aqua Regia and acid digestion on 260 samples selected from

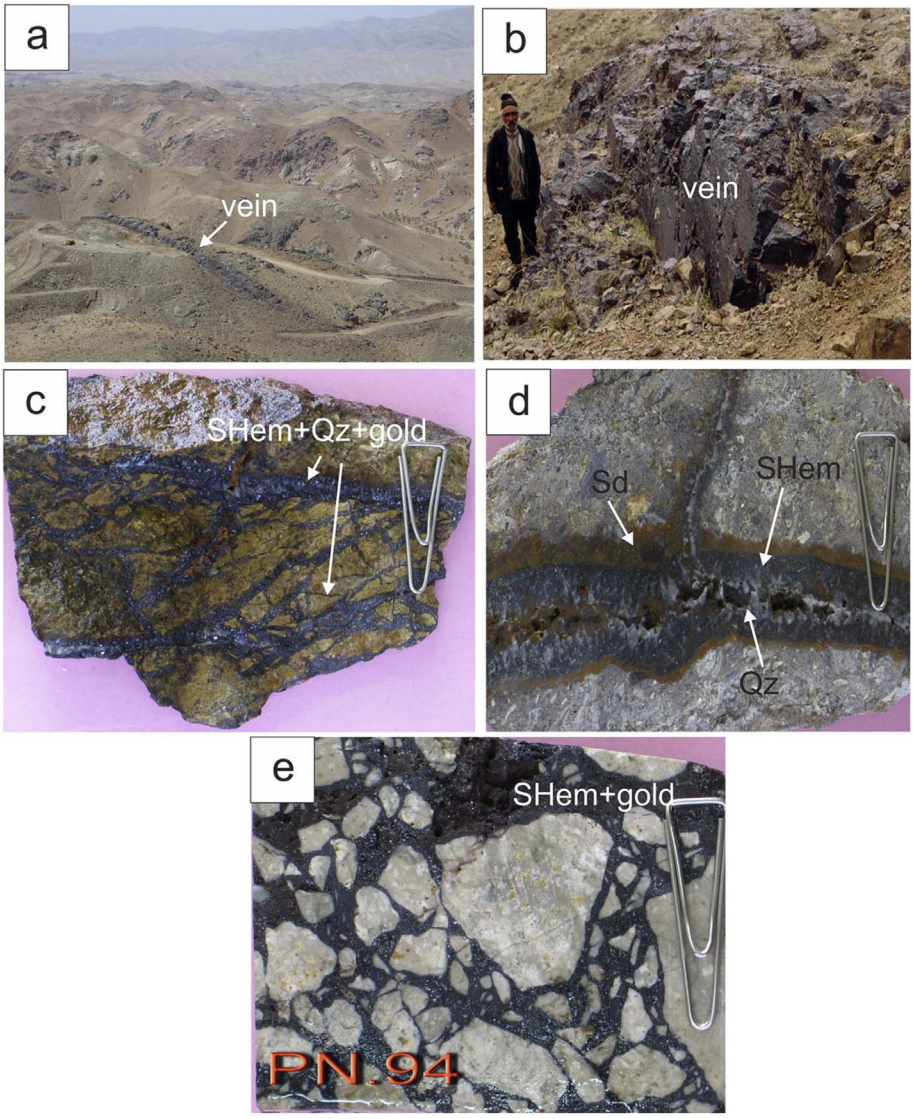

Fig. 6. a. Vein-type mineralization in fault zone at Mohammad Baigi mineralized zone (looking to NW). b. Specular hematite–gold–quartz vein in Tangeh Piazi mineralized zone. c. Stockwork-like texture bearing specular hematite-quartz-gold veinlets. d. Open space filling texture in the veinlet ores. e. Hydrothermal breccia consists of brecciated fragments of the altered host rock cemented by specular hematite and gold. (Qz: quartz, SHem: specular hematite, Sd: siderite (Whitney and Evans, 2010).)

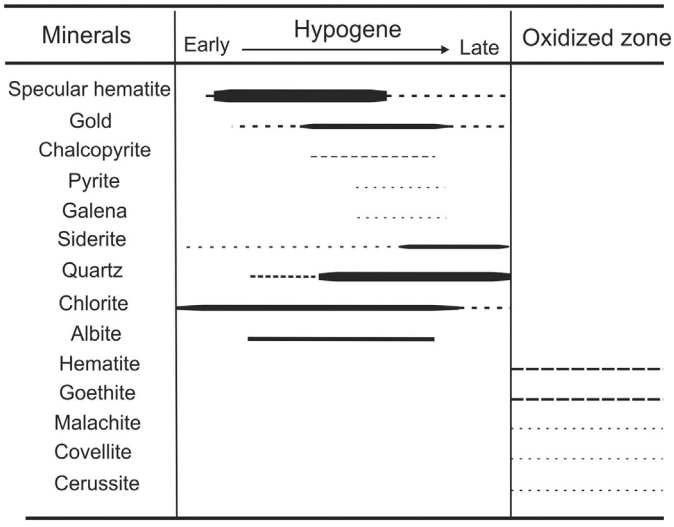

Fig. 7. Paragenetic sequence of mineral assemblages in the Kuh-e-Zar deposit.

mineralized zones by Zarmehr Company.

Twenty one doubly polished wafers (150 μm thick) prepared for fluid inclusion studies were examined petrographically. Thirteen wafers containing suitable fluid inclusions (> 5 μm in size) were selected for microthermometric measurements from quartz in different mineralized zones with variation in mineral assemblage. The measurements were conducted on a Linkam THMSG 600 heating-freezing stage with temperature limits of 600 °C and −190 °C, and a precision of ± 1.0 °C (www.lab.umcs.lublin.pl/THMS600_linkam.pdf).

Five samples of quartz and chalcopyrite from the Tarik Darreh and Farshami mineralized zones were analyzed for stable isotope (oxygen and sulfur) compositions after careful hand picking and purification at the Institute of Mineralogy and Geochemistry, University of Lausanne, Switzerland. Oxygen isotopic measurements were obtained using protocols from Sharp (1990), Rumble and Hoering (1994), and Kasemann et al. (2001). The V-SMOW ($\delta^{18}O$ SMOW) values were established relative to an internal standard NBS–28 quartz ($\delta^{18}O$ = 9.64 ± 0.06‰). The S-isotope compositions were measured in automated fashion using a Carlo Ebra (1100 CE) elemental analyzer linked to a Finnigan Delta S mass spectrometer. The samples were calibrated against IAEA standards S1 and S3 (Ag_2S) and NBS-127 ($BaSO_4$) with accepted values of −0.3, −32.1, and 20.3‰, respectively.

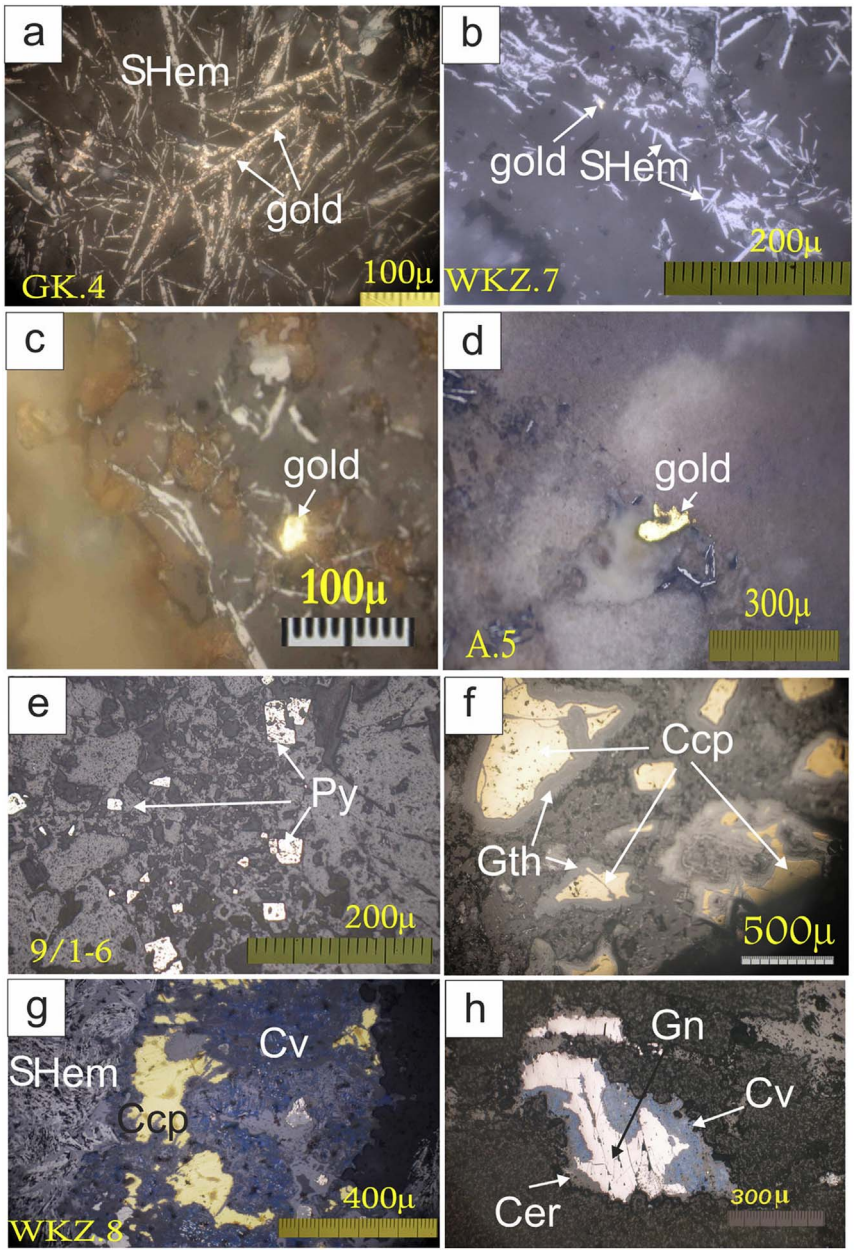

Fig. 8. Photomicrographs of ore minerals from the Kuh-e-Zar deposit (polished blocks, reflected light, in air). a. Specular hematite blades and fine-grained gold between them. b. Fine-grained specular hematite and gold grains. c and d. Corse-grained gold from the Mohammad Biagi and Alireza mineralized zones. e. Disseminated pyrite in quartz veinlet. f. Chalcopyrite crystal replaced by goethite along borders. g. Chalcopyrite crystal replaced by covellite along borders. h. Cerussite occurrences along borders and fracture planes. Covellite occurs at contact between galena and gangue minerals. (SHem: specular hematite, Py: pyrite, Gth: goethite, Ccp: chalcopyrite, Cv: covellite, Gn: galena, Cer: cerussite (Whitney and Evans, 2010).)

6. Geochemistry, U-Pb dating, and Sr-Nd-Pb isotopes

6.1. Whole rock geochemistry

Representative whole rock analyses of the Kuh-e-Zar intrusive rocks are shown in Table 2. The SiO_2 contents and total alkali ($Na_2O + K_2O$) range from 55.5 to 73.1 wt% and 5.3 to 9 wt%, respectively (Fig. 10a). According to the SiO_2 vs. total alkali diagram (Middlemost, 1994), the samples are quartz monzonite, quartz monzodiorite, granite, and granodiorite (Fig. 10a). The K_2O contents are between 3.18 and 5.7 wt %. Kuh-e-Zar granitoids are high-K calc-alkaline to shoshonitic intrusions (Table 2 and Fig. 10b). The Kuh-e-Zar intrusive rocks belong to the metaluminous to peraluminous granitoid series, with A/CNK < 1.3 (molar $Al_2O_3/(CaO + K_2O + Na_2O)$). In the Rb versus Ta + Yb diagram (Pearce et al., 1984), these rocks show affinities to volcanic arc granites (VAG); however, syenogranitic rock also straddles the boundary to the syn-collision granites (Fig. 10c and d).

The chondrite-normalized REE patterns (Fig. 11a) are characterized by LREE moderate enrichment ($(La/Yb)_N$ = 7–8.72), HREE depletion and mostly negative Eu anomalies (0.63–1.03) (Table 2 and Fig. 11a). The syenogranitic rock is characterized by lower total REE concentration than the granodiorite, quartz monzonite, and quartz monzodiorite (Table 2 and Fig. 11a). Primitive mantle-normalized trace element spider diagrams (Sun and McDonough, 1989) show enrichment in large-ion-lithophile elements (LILE), such as K, Rb, Ba and Cs, and other incompatible elements (Th and U). The most characteristic high-field-strength elements (HFSE) – e.g. Nb, Zr, Y, Ti and HREE – have, compared to LILE, lower normalized values; in particular, there are steep negative anomalies in Nb (Fig. 11b). These features are typical of the subduction-related magmas, namely in the calc-alkaline volcanic arcs of continental active margins (Gill, 1981; Pearce, 1983; Wilson, 1989; Walker et al., 2001). Although, in general, as already described, LILE are enriched relative to HFSE, syenogranitic rock display lower total normalized values than the other intrusions (Fig. 11b).

6.2. Zircon U-Pb geochronology of intrusive rocks

The LA-ICPMS zircon U–Pb dating results of the biotite-hornblende

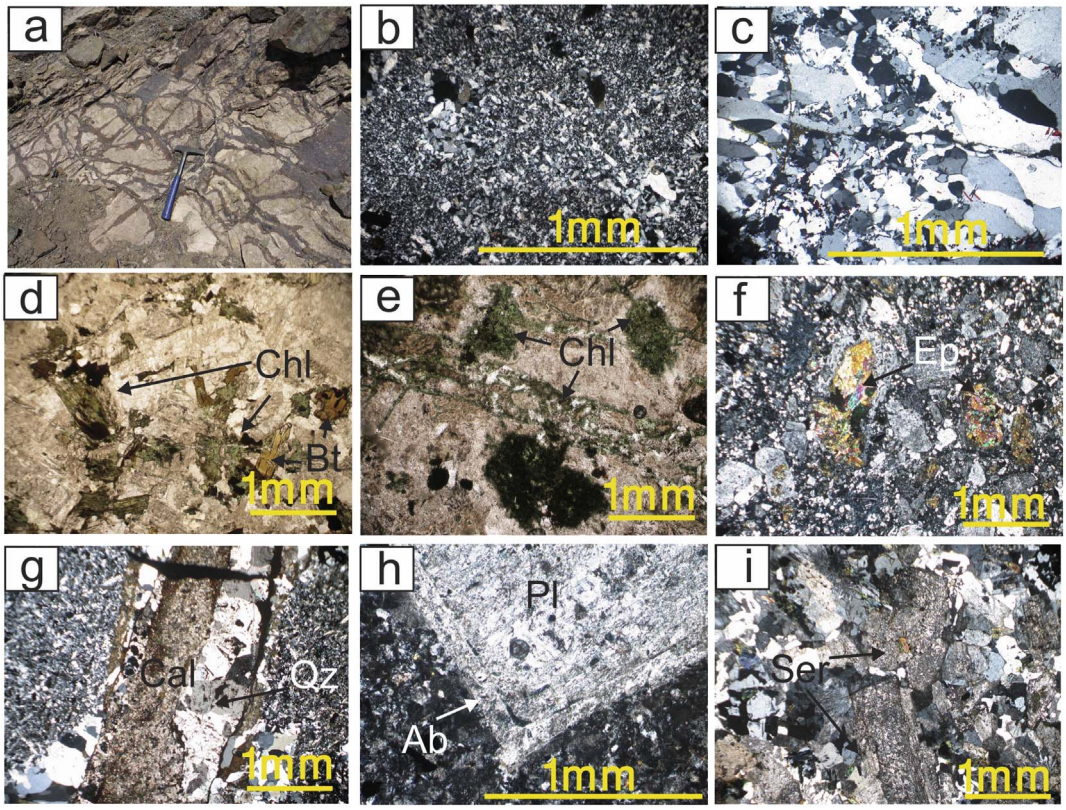

Fig. 9. Photomicrographs of hydrothermal alteration assemblages from the Kuh-e-Zar deposit. a. Silicification alteration associated with mineralized zone as quartz-specular hematite ± gold veinlets. b. Silicification of host rock in the Ghar-e-Kaftari zone (XPL). c. Coarse-grained quartz veinlet in the Tarik Darreh zone (XPL). d. Replacement of biotite by chlorite in propylitic alteration (PPL). e. Chlorite as quartz-chlorite veinlet and replacement of mafic minerals (PPL). f. Plagioclase is altered to epidote in propylitic zone (XPL). g. Quartz-calcite veinlet in propylitic alteration (XPL). h. Replacement of plagioclase by albite in margin within quartz monzodiorite unit (XPL). i. Plagioclase is altered to sericite in syenogranite unit (XPL). Qz: quartz, Chl: chlorite, Bt: biotite, Ep: epidote, Cal: calcite, Ab: albite, Pl: plagioclase, Ser: sericite (Whitney and Evans, 2010).

quartz monzodiorite porphyry (sample MKZ-7) and biotite-hornblende quartz monzonite porphyry (sample MKZ-13) are summarized in Table 3 and illustrated in Figs. 12 and 13. In all the dated samples, the zircon grains are colorless and/or pale yellow, transparent and commonly euhedral. The grain sizes range from 50 to 300 μm; the grains have a length/width ratio of 1:1 to 5:1. The result of the calculation of the isotopic age of the biotite-hornblende quartz monzodiorite porphyry (sample MKZ-7) and biotite-hornblende quartz monzonite porphyry (sample MKZ-13) are presented as concordia and best age graphics (Figs. 12 to 13). Analysis of biotite-hornblende quartz monzodiorite porphyry yielded a mean age (weighted mean) of 41.2 ± 2.1 Ma (Table 3; 10 analyzed points, errors shown are 2σ). The mean age (weighted mean) of the biotite-hornblende quartz monzonite porphyry is 40.9 ± 3.1 Ma (Table 3; 13 analyzed points, errors shown are 2σ). The relatively invariable U/Th ratios and their respective spot U-Pb ages (Table 3) are consistent with magmatic zircons, and no inherited components were detected. These characteristics together with the high closure temperatures of zircon (e.g., Cherniak and Watson, 2000) indicate the U–Pb data as representative of the crystallization ages of the respective igneous rocks. Therefore, the U–Th–Pb zircon dating indicates that both granodiorite and quartz monzonite rocks intruded in the middle Eocene (Lutetian) time.

6.3. Whole rock Sr-Nd-Pb isotopes

Sr, Nd, and Pb isotopic analyses of Kuh-e-Zar intrusions were performed on one biotite-hornblende quartz monzodiorite porphyry sample (MKZ-7), two biotite-hornblende quartz monzonite porphyry samples (MKZ-13 and MKZ-20), one syenogranite sample (MKZ-11), and one hornblende-biotite granodiorite sample (FZ-56). The results are shown in Table 4. The initial isotopic compositions are back-projected at an age of ≈ 41 Ma (Table 4), which is the age obtained from zircon geochronology of the intrusions (see Section 6.2). The age-corrected initial $^{87}Sr/^{86}Sr$ isotope ratio of the biotite-hornblende quartz monzodiorite porphyry is 0.706355. Initial $^{143}Nd/^{144}Nd$ ratio and εNd(t) are 0.512500 and −1.68, respectively. The sample shows Pb isotope compositions with $^{206}Pb/^{204}Pbi$ = 18.69, $^{207}Pb/^{204}Pbi$ = 15.62, and $^{208}Pb/^{204}Pbi$ = 38.85. The two biotite-hornblende quartz monzonite porphyry samples have initial $^{87}Sr/^{86}Sr$ ratios of 0.705488 from 0.705963, initial $^{143}Nd/^{144}Nd$ ratios from 0.512434 to 0.512537 with εNd(t) ranging from −0.96 to −2.93, $^{206}Pb/^{204}Pbi$ ratios from 18.60 to 18.62, $^{207}Pb/^{204}Pbi$ ratios from 15.60 to 15.63, and $^{208}Pb/^{204}Pbi$ ratios from 38.74 to 38.78. The syenogranite and hornblende-biotite granodiorite samples have Sr–Nd–Pb isotope compositions similar to those of the quartz monzodiorite porphyry and quartz monzonite porphyry samples: $^{87}Sr/^{86}Sri$ = 0.706408 and 0.706033, $^{143}Nd/^{144}Ndi$ = 0.512583 and 0.512476, εNd(t) = −0.06 and −2.14, $^{206}Pb/^{204}Pbi$ = 18.62 and 18.71, $^{207}Pb/^{204}Pbi$ = 15.66 and 15.63, and $^{208}Pb/^{204}Pbi$ = 39.24 and 38.96, respectively (Table 4). In the εNd versus initial $^{87}Sr/^{86}Sr$ diagram (Fig. 14a), these rocks plot to the right of the so called mantle array and field of island-arc basalts, which suggests that continental crust was involved in generating the acidic-intermediate magmas.

The age of crustal extraction of the intrusive rocks at Kuh-e-Zar can also be estimated with the Nd mean crustal residence age (TDM), which approximates the time of Sm/Nd fractionation associated with partial melting of depleted mantle to form juvenile Arabian-Nubian Shield (ANS) crust. The DePaolo (1981) model is used here, because it is more appropriate than the model provided by Goldstein et al. (1984) for calculating crustal extraction ages generated in arc-like tectonic settings (Dickin, 2005). These TDM ages (0.70–0.98 Ga) indicate the predominance of the Neoproterozoicas the crustal source of the Kuh-e-Zar

Table 2
Major, trace, and REE elements analysis of least–altered intrusive rocks from the Kuh-e-Zar area.

Wt%	Mkz-13	Mkz-24	Mkz-7	Mkz-9	Mkz-27	Mkz-18	mkz-21	Mkz-5	Mkz-11	Fz-56	Mkz-26	Mkz-20	Mkz1-1
Rock type	1	1	2	2	2	2	2	3	3	4	4	1	1
wt%													
SiO_2	64.12	63.33	57.38	61.38	62.18	55.49	57.69	68.25	69.1	63.55	64.48	61.69	64.12
TiO_2	0.84	1.10	2.11	1.10	0.98	1.96	1.10	0.48	0.74	0.47	0.83	0.94	0.82
Al_2O_3	15.07	14.92	14.92	15.31	14.63	15.56	14.63	13.79	13.68	15.68	15.5	13.79	13.94
FeOT	4.90	6.52	7.68	6.50	5.35	8.50	7.21	5.11	4.96	5.39	5.31	5.93	4.06
MnO	0.18	0.25	0.26	0.33	0.15	0.33	0.18	0.17	0.19	0.19	0.19	0.18	0.19
MgO	2.20	2.70	3.34	1.51	2.27	3.56	3.04	1.92	1.24	2.94	2.58	2.54	2.23
CaO	1.65	0.99	4.98	3.85	4.78	5.92	6.57	0.68	0.67	2.14	2.53	4.15	3.59
Na_2O	4.70	3.43	2.72	2.67	3.03	2.11	3.04	2.75	1.88	3.25	3.54	3.49	3.73
K_2O	4.04	4.56	3.51	4.16	4.12	3.18	3.47	4.71	5.70	3.75	3.61	4.19	4.00
P_2O_5	0.19	0.15	0.24	0.19	0.17	0.24	0.20	0.06	0.15	0.17	0.17	0.18	0.15
L.O.I.	1.67	2.00	2.73	2.15	1.53	2.53	2.23	1.20	0.95	1.47	1.07	2.25	2.37
Total	99.56	99.95	99.87	99.15	99.19	99.85	99.36	99.12	99.26	99.00	99.81	99.33	99.20
ppm													
V	82		176		145	200	158		74	93	107		
Cr	6				22	53			11		93		
Co	37.0		36.8		46.0	37.0	28.6		50.0	8.5	11.0		
Ni	29				37	45			32		33		
Cs	1.2		10.2		2.5	5.6	3.8		1.2	2.7	6.5		
Ba	1158		605		465	433	530		929	753	532		
Rb	86.0		81.9		102.0	75.0	106.3		166.0	88.9	89.0		
Sr	166.0		347.6		331.0	300.0	431.9		57.0	170.5	229.0		
Y	22.0		17.1		20.0	21.0	20.8		9.0	21.4	18.0		
Zr	212.0		179.4		22.0	8.0	177.9		19.0	167.3	54.0		
Nb	11.0		9.7		10.0	9.0	9.1		6.0	7.9	8.0		
Hf	5.5		4.4		0.7	0.3	4.8		0.7	4.4	1.7		
Ta	1.4		1.2		1.4	1.0	1.0		1.3	0.6	0.6		
Pb	4.8				11.1	19.1			8.3		7.7		
Th	9.2		6.1		9.7	6.3	9.7		7.3	9.7	8.1		
U	1.9		1.2		1.5	1.0	2.5		0.7	1.8	1.4		
La	26.9		22.7		22.8	21.2	24.7		11.4	26.5	23.3		
Ce	48.6		43.6		46.8	47.1	47.9		24.0	51.3	47.8		
Pr	5.54		4.90		5.35	5.34	5.49		2.73	5.49	5.12		
Nd	21.2		18.6		21.3	21.3	20.8		10.3	20.4	9.4		
Sm	4.11		3.73		4.18	4.64	4.13		2.26	4.00	3.98		
Eu	0.83		1.22		0.89	1.10	0.92		0.47	0.92	0.91		
Gd	4.00		3.51		4.54	5.18	4.06		2.27	3.78	4.25		
Tb	0.58		0.50		0.59	0.60	0.60		0.27	0.59	0.52		
Dy	3.50		3.09		3.67	4.05	3.77		1.59	3.79	3.15		
Ho	0.71		0.59		0.65	0.74	0.74		0.39	0.72	0.58		
Er	2.04		1.66		2.00	2.14	2.20		0.94	2.07	1.81		
Tm	0.36		0.27		0.26	0.25	0.36		0.08	0.35	0.19		
Yb	2.23		1.85		1.97	1.94	2.38		0.88	2.26	1.83		
Lu	0.35		0.30		0.24	0.25	0.35		0.10	0.34	0.22		
Ratios													
Sr/Y	7.7		20.3		16.7	14.5	20.7		6.5	7.9	12.8		
Eu/Eu[a]	0.63		1.03		0.63	0.68	0.69		0.63	0.72	0.68		
$(La/Yb)_N$	8.13		8.27		7.78	7.37	7.00		8.72	7.91	8.56		

1-Bt-Hbl quartz monzonite porphyry, 2-Bt-Hbl quartz monzodiorite porphyry, 3-Syenogranite, 4-Hbl-Bt granodiorite.
$(La/Yb)_N$ = La normalized by chondrite/Yb normalized by chondrite.
[a] X-ray fluorescence analysis of major elements was performed at the Ferdowsi University of Mashhad, using a Philips PW1480 X-ray spectrometer. Trace elements and REE analyses were carried out at the ACME laboratory of Canada using ICP-MS and the following lithium metaborates/tetraborates fusion and nitric acid digestion of a 0.2 g sample.

intrusions (Table 4).

The narrow range of Pb isotope data ($^{206}Pb/^{204}Pbi$ = 18.6–18.7 (Fig. 14b))shows a relative isotopic homogeneity of the mantle source. In the $^{207}Pb/^{204}Pbi$ and $^{208}Pb/^{204}Pbi$ versus $^{206}Pb/^{204}Pbi$ plots (Fig. 14b and c), all the intrusive rocks plot between the enriched mantle reservoirs (EMI and EMII) and Atlantic and Pacific MORB trends and in the field of upper crust, above the Northern Hemisphere Reference Line (NHRL, Zindler and Hart, 1986).

7. Fluid inclusion studies

7.1. Morphology and inclusion type

Heating and freezing tests were made on primary fluid inclusions (based on criteria given by Roedder, 1984) in quartz within quartz–-specular hematite–gold, quartz–specular hematite–gold ± pyrite ± chalcopyrite, and quartz–specular hematite–gold ± siderite veins. Primary fluid inclusions are abundant. They have small size (typically 3–12 μm, average 7 μm) in quartz samples (Fig. 15). Fluid inclusion shapes are elliptical, irregular, and some directional elongated. Fluid inclusions were issued as clusters, single inclusions, linear arrays, and along fractures or grain boundaries. The type of inclusions is two-phase, liquid-rich with 5–20% vapor in volume percentage, which homogenize into a liquid state upon heating (Fig. 15). The missing of liquid CO_2 or clathrate formation during freezing experiments proposes that none of the inclusions contained significant quantities of CO_2. Also, fluid inclusion evidence for a fluid boiling process in the Kuh-e-Zar samples is not clear.

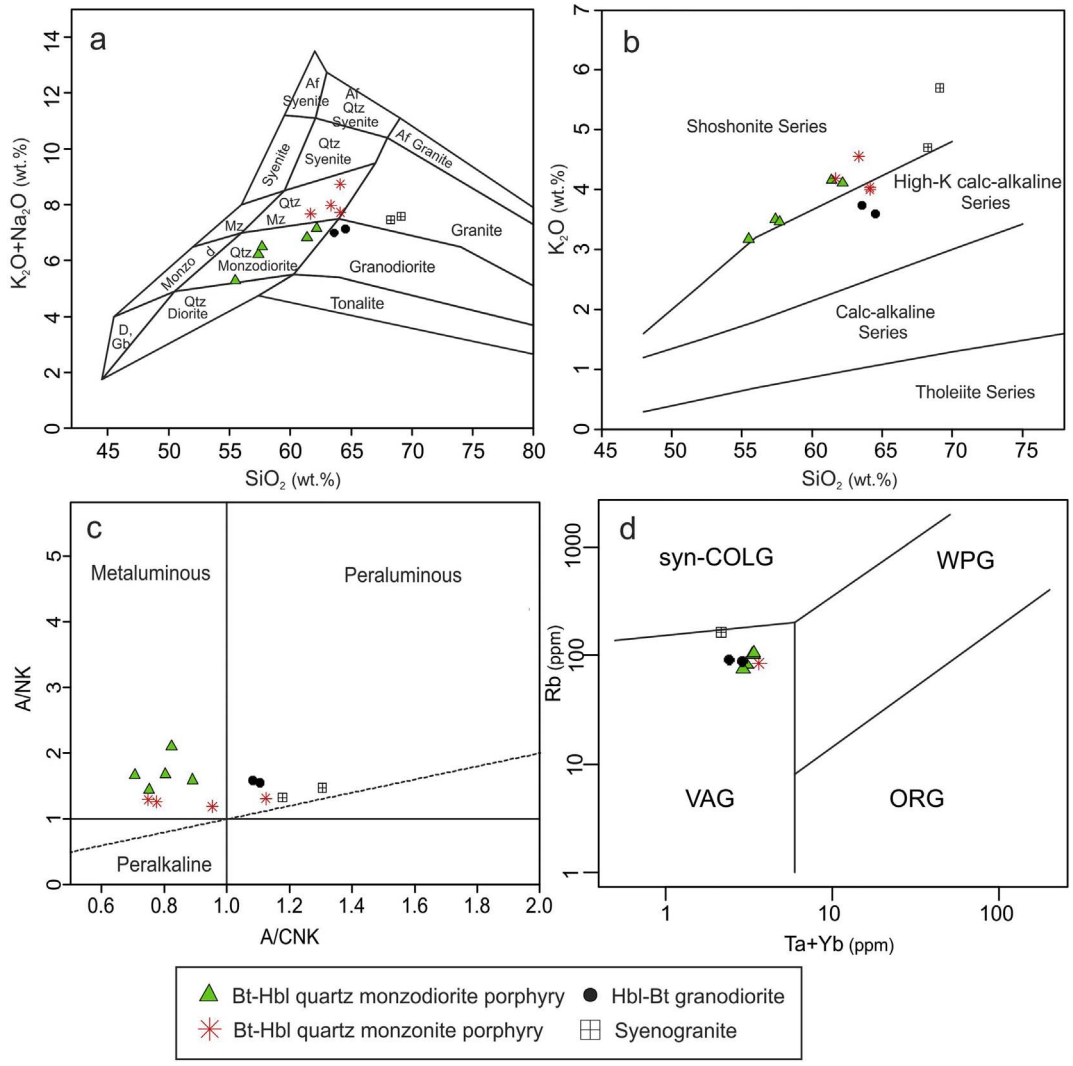

Fig. 10. a. Na_2O + K_2O vs. SiO_2 classification diagram (Middlemost, 1994) for Kuh-e-Zar granitoids, b. K_2O vs. SiO_2 diagram for discrimination of tholeiite, calk-alkaline, and shoshonite series (Peccerillo and Taylor, 1976). The Kuh-e-Zar intrusions mostly plot in the high-K calk-alkaline and shoshonite fields, c. A/NK (molar Al_2O_3/Na_2O + K_2O) vs. A/CNK (molar Al_2O_3/CaO + Na_2O + K_2O) diagram (Maniar and Piccoli, 1989) for Kuh-e-Zar granitoids, d. Rb vs. Ta + Yb discrimination diagram (Pearce et al., 1984) showing the tectonic setting of the intrusive rocks of Kuh-e-Zar deposit. WPG: within plate granitoid; Syn-COLG: syn-collisional granitoid; ORG: ocean ridge granitoid; VAG: volcanic arc granitoid.

7.2. Microthermometric measurements

Homogenization temperatures (T_h) values range from 248 to 491 °C (average 369 °C, n = 102) in quartz–specular hematite–gold veins, 271 to 384 °C (average 350 °C, n = 40) in quartz–specular hematite–-gold ± pyrite ± chalcopyrite veins, and 320 to 368 °C (average 345 °C, n = 22) in quartz–specular hematite–gold ± siderite veins (Table 5 and Fig. 16a). These T_h values indicate a minimum temperature at which the hydrothermal fluid is trapped in the inclusion. The precise pressure during mineralization is unknown in the area. The average T_h values of primary inclusions in different veins indicate that the temperature of the mineralizing fluids was slightly higher during quartz–specular hematite–gold veins precipitation, and decreased to quartz–specular hematite–gold ± pyrite ± chalcopyrite and quartz–-specular hematite–gold ± siderite veins precipitation. The results of microthermometric measurements confirm that the deposit can be classified as a medium- to high-temperature deposit.

The first melting temperatures (T_{fm}) values of primary inclusions in different veins cluster between − 55.4 and − 57.6 °C (average − 56.8 °C, n = 164). They indicate hydrothermal fluids containing salts of $CaCl_2$ and NaCl in comparison with the values to the eutectic temperatures of various water-salt systems (Shepherd et al., 1985; Gokce, 2000). No difference between samples collected from different veins was detected; this indicates that the salt composition of the fluid was homogenous during earlier and later mineralizing episodes.

The final ice melting temperatures ($T_m$ice) values range from − 4.1 to − 15.7 °C (average − 8.03 °C, n = 51) in quartz–specular hematite–gold veins, − 2.4 to − 7.8 °C (average − 4.91 °C, n = 31) in quartz–specular hematite–gold ± pyrite ± chalcopyrite veins, and − 3.1 to − 4.5 °C (average − 3.79 °C, n = 9) in quartz–specular hematite–gold ± siderite veins (Table 5 and Fig. 16b). The salinities of the hydrothermal fluids were calculated using the equation by Bodnar (1993), and yielded wt% NaCl equivalents as follows: 6.3 to 19.2 wt% NaCl equivalent (average 11.4 wt% NaCl equivalent, n = 51) in quartz–specular hematite–gold veins, 4 to 11.4 wt% NaCl equivalent (average 7.6 wt% NaCl equivalent, n = 31) in quartz–specular hematite–gold ± pyrite ± chalcopyrite veins, and 5.1 to 7.1 wt% NaCl equivalent (average 6.1 wt% NaCl equivalent, n = 9) in quartz–specular hematite–gold ± siderite veins (Table 5 and Fig. 16c). The average salinity values of primary inclusions in different veins indicate that the salinity of the mineralizing fluids was slightly higher during quartz–specular hematite–gold vein precipitation, and decreased to quartz–specular hematite–gold ± pyrite ± chalcopyrite and

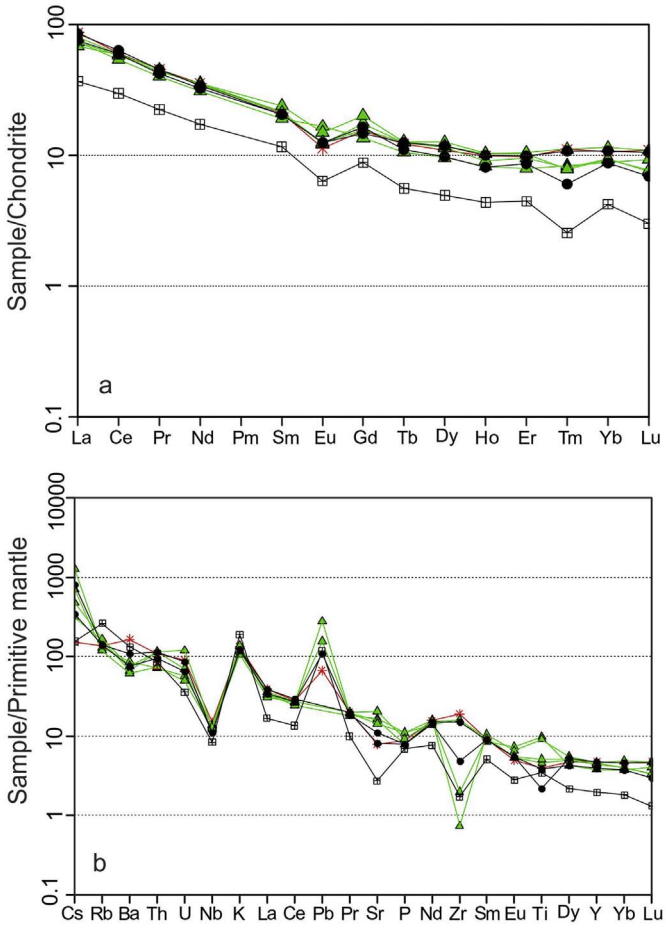

Fig. 11. a. Chondrite-normalized rare earth elements and b. primitive mantle normalized trace element patterns for the Kuh-e-Zar granitoids.
(Chondrite and primitive mantle values are from Boynton (1985) and Sun and McDonough (1989), respectively.)

quartz–specular hematite–gold ± siderite veins precipitation (Fig. 16c). These salinity data demonstrate that the ore-forming fluids were medium- to low-salinity fluids.

8. Stable isotope

Two quartz samples from the Tarik Darreh zone (quartz ± specular hematite ± gold ± chalcopyrite vein) were used for oxygen isotope studies. The $\delta^{18}O$ values of the quartz samples vary from 13.2 to 13.7‰ relative to Standard Mean Ocean Water (SMOW) with a mean of 13.45‰ (Table 6) and are similar to those of magmatic rocks (Hoefs, 1984). These results may suggest a magmatic source. However, this conclusion, without having δD data, was drawn with trepidation. The $\delta^{18}O$ values for water in equilibrium with quartz were calculated using the equation of Zhang et al. (1989) and the average homogenization temperature values obtained during our fluid inclusion studies (350 °C). These estimated $\delta^{18}O$ values vary in a narrow range from +7.4 to +7.9‰ (SMOW) (Table 6). The results associated with T_h values (average 350 °C) show that the ore-forming fluids isotopically possessed dominantly magmatic characteristics during the formation of the Tarik Darreh vein.

According to Ohmoto (1972) and Ohmoto and Goldhaber (1997), the sulfur isotopic compositions of metallic minerals ($\delta^{34}S$) and ore-forming fluids ($\delta^{34}S_{\Sigma S}$) make constraints on possible geological sources of sulfur and other metallogenic elements, and help to decipher the conditions of formation of sulfides in ore deposits. Three chalcopyrite samples from the Tarik Darreh and Farshami zones (quartz-chalcopyrite ± specular hematite ± gold ± pyrite vein) were used for sulfur isotope studies. The sulfur isotopic compositions (i.e. $\delta^{34}S$) of these samples were −2.4 to +1.0‰ relative to Canion Diablo Troilite (CDT). In term of $\delta^{34}S$ values, there is not a significant difference between the analyzed samples. The $\delta^{34}S_{CDT}$ values of H_2S in equilibrium with chalcopyrite were estimated to be in the range of −2.5 to +0.9‰ by evaluating the $\delta^{34}S$valuesof chalcopyrite with the average temperature of the hydrothermal fluid during the chalcopyrite mineralization episode taken to be 350 °C (determined by homogenization temperature measurements during fluid inclusion studies in the quartz samples as closely relationship with chalcopyrite), using the equation suggested by Li and Liu (2006) (Table 6).

Table 3
Results of U-Pb-Th laser-ablation multicollector ICP mass spectrometry analysis of zircon from the Kuh-e-Zar intrusions.

Analysis	U (ppm)	$^{206}Pb/^{204}Pb$	U/Th	$^{206}Pb/^{207}Pb$	± (%)	$^{207}Pb/^{235}U$	± (%)	$^{206}Pb/^{238}U$	± (%)	Age (Ma)	± (m.y.)
MKZ-7 (Bt-Hbl quartz monzodiorite porphyry)											
1	130	2444	1.9	31.8932	58.9	0.0261	60.5	0.0060	13.7	38.7	5.3
2	153	9495	2.3	15.7493	78.8	0.0532	79.9	0.0061	13.0	39.1	5.1
3	106	3370	2.4	5.8741	209.9	0.1443	210.2	0.0061	11.4	39.5	4.5
4	198	3312	1.6	25.7516	50.1	0.0330	50.5	0.0062	6.4	39.6	2.5
5	255	5872	0.7	19.4879	40.5	0.0443	41.3	0.0063	8.0	40.2	3.2
6	110	3373	1.4	7.3843	150.9	0.1189	151.7	0.0064	15.4	40.9	6.3
7	220	6054	0.6	11.6286	142.4	0.0755	142.5	0.0064	6.1	40.9	2.5
8	333	6529	1.3	21.6258	35.5	0.0414	35.9	0.0065	5.4	41.7	2.2
9	133	3692	1.3	29.6789	75.2	0.0310	76.6	0.0067	14.6	42.8	6.2
10	222	3864	2.2	25.4216	38.4	0.0369	38.8	0.0068	5.2	43.7	2.3
MKZ-13 (Bt-Hbl quartz monzonite porphyry)											
1	107	2693	1.2	3.2639	610.0	0.2550	610.2	0.0060	14.8	38.8	5.7
2	151	3074	2.1	23.5444	65.9	0.0359	66.9	0.0061	11.8	39.4	4.6
3	255	7663	1.4	23.6292	37.4	0.0363	38.2	0.0062	7.5	40.0	3.0
4	135	4467	1.3	22.0409	63.5	0.0393	66.0	0.0063	17.8	40.4	7.2
5	143	7189	1.1	15.6005	40.6	0.0564	42.7	0.0064	13.1	41.0	5.3
6	244	1549	1.0	27.0668	47.1	0.0326	47.9	0.0064	8.6	41.1	3.5
7	94	3038	1.3	7.6002	125.1	0.1166	125.9	0.0064	14.2	41.3	5.8
8	64	2239	1.4	9.3578	60.6	0.0956	63.6	0.0065	19.3	41.7	8.0
9	79	2677	1.3	5.2539	243.1	0.1713	243.5	0.0065	14.8	41.9	6.2
10	65	1218	1.3	5.9463	87.1	0.1538	88.7	0.0066	16.9	42.6	7.2
11	94	2155	1.2	13.7522	80.6	0.0668	82.4	0.0067	17.0	42.8	7.3
12	78	2516	1.4	3.2591	288.6	0.2875	289.3	0.0068	20.4	43.7	8.9
13	71	1818	1.4	14.4555	73.7	0.0679	76.1	0.0071	19.0	45.7	8.6

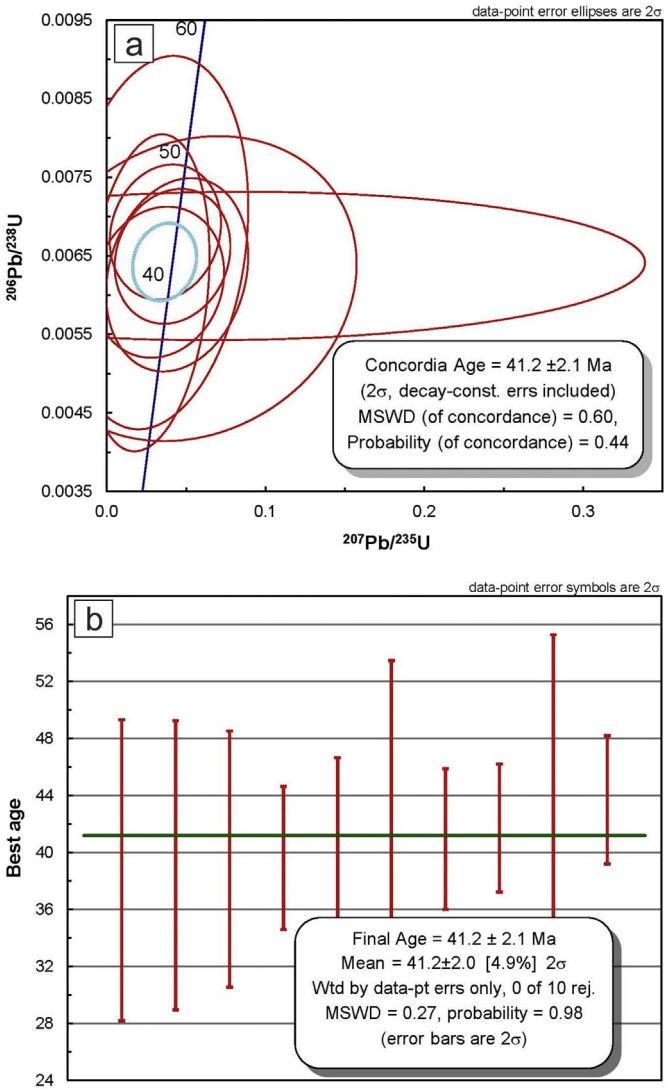

Fig. 12. Zircon U-Pb dating of representative rock sample from the biotite-hornblende quartz monzodiorite porphyry unit (sample MKZ-7). a) Concordia diagram, b) best age plot.

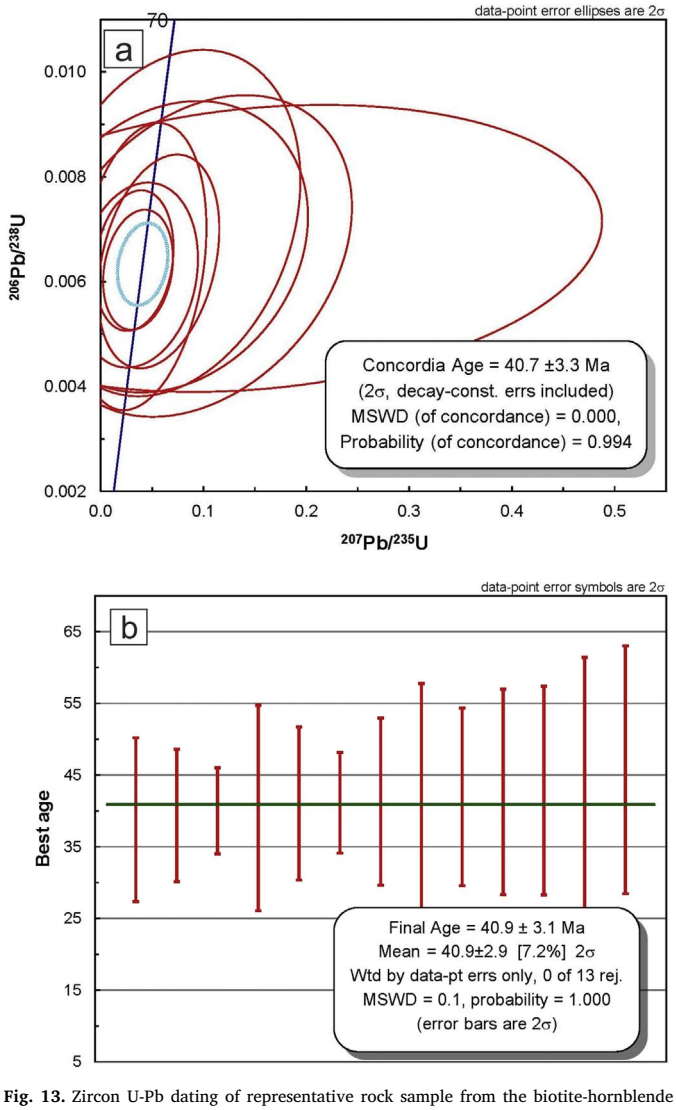

Fig. 13. Zircon U-Pb dating of representative rock sample from the biotite-hornblende quartz monzonite porphyry unit (sample MKZ-13). a) Concordia diagram, b) best age plot.

9. Discussion

9.1. Magma source and petrogenesis of intrusive rocks

The Kuh-e-Zar middle Eocene intrusions are subduction-related calc-alkaline igneous rocks with isotopic evidence showing mantle-derived magmas that interacted with continental crust. Their strong geochronology and geochemistry resemblance to each other suggests that the granodiorite, quartz monzonite, and quartz monzodiorite intrusives are genetically related and most likely derived from the same initial melt. The Kuh-e-Zar intrusions contain biotite, magnetite, and hornblende, and mostly vary from metaluminous to peraluminous (A/CNK < 1.1), as expected for I-type granitoids (Chappell and White, 2001). The studied rocks also display enrichment of LILEs (Cs, Rb, Ba, and K) and LREEs (La and Ce), depletion of HFSEs (Nb, Zr, Y, and Ti) and HREEs (Yb and Lu), and negative Eu anomalies. These characteristics demonstrate that subduction played a dominant role in their petrogenesis (Wilson, 1989; Walker et al., 2001). Based on low $(La/Yb)_N$ ratios (< 9.07) and high Yb_N contents (mainly > 8), the most samples are plotted in the field of classic island arc and different from adakites (Fig. 17).

The very similar initial Sr, Nd, and Pb isotope compositions in these five samples suggests that most of the Kuh-e-Zar intrusions are co-genetic, deriving from the same parental magmas by magmatic differentiation processes, such as crystal fractionation. The source of the magma can be find out based on εNd(t) values, if it is negative the magma originated from the continental crust and positive from mantle (Yang et al., 2007; Kemp et al., 2007; Li et al., 2009; Girardi et al., 2012). Based on the εNd(t)–($^{87}Sr/^{86}Sr$)i isotopic plot (Fig. 14a), the Kuh-e-Zar granitoid rocks exhibit a trend toward the upper continental crust, suggesting that crustal contamination played a role in magma evolution (Kemp et al., 2007; Li et al., 2009). According to Zhou et al. (2004), the contamination by continental crust material within the magma chamber would lead to the coupled enrichment in highly incompatible mobile LILEs (e.g., Rb, K). In addition, the negative Nb anomalies in the primitive mantle normalized multi-element spectra is a typical character of rocks formed in a supra-subduction setting (Pearce and Cann, 1993). Therefore, crustal contamination can be confirmed in their genesis. The values of $^{206}Pb/^{204}Pb_i$, $^{207}Pb/^{204}Pb_i$ and $^{208}Pb/^{204}Pb_i$ in the Kuh-e-Zar intrusive rocks are consistent with this claim (Fig. 14b and c).

According to Tatsumi and Takahashi (2006), generation of magma in a subduction-related environment can be triggered by partial melting of mantle wedge peridotite metasomatized by a slab-derived fluid or partial melting of oceanic slab itself. The direct melting of the oceanic

Table 4
Rb–Sr, Sm–Nd whole rock data and Pb-isotope ratios obtained from monzonites, granodiorite, syenogranite, and monzodiorite samples from the Kuh-e-Zar area. Analytical methods are described in Section 5.

Sample	$^{147}Sm/^{144}Nd$	$^{143}Nd/^{144}Nd$ (m)	$^{143}Nd/^{144}Nd$ (Unc)	$^{143}Nd/^{144}Nd$ (i)	εNd	TDM	$^{87}Rb/^{86}Sr$	$^{87}Sr/^{86}Sr$ (m)	$^{87}Sr/^{86}Sr$ (Unc)	$^{87}Sr/^{86}Sr$ (i)	$^{206}Pb/^{204}Pb$ (i)	$^{207}Pb/^{204}Pb$ (i)	$^{208}Pb/^{204}Pb$ (i)
MKZ-11	0.1179	0.512614	0.000012	0.512583	− 0.06	0.70	0.0850	0.706457	0.000007	0.706408	18.62	15.66	39.24
MKZ-7	0.1178	0.512531	0.000012	0.512500	− 1.68	0.82	0.6322	0.706719	0.00001	0.706355	18.69	15.62	38.85
MKZ-20	0.1258	0.512570	0.000012	0.512537	− 0.96	0.83	0.7384	0.705913	0.000012	0.705488	18.62	15.60	38.74
MKZ-13	0.1241	0.512468	0.000009	0.512434	− 2.93	0.98	1.4753	0.706828	0.000016	0.705963	18.60	15.63	38.78
FZ-56	0.1207	0.512508	0.000012	0.512476	− 2.14	0.88	1.5242	0.706910	0.000012	0.706033	18.71	15.63	38.96

m: measured, Unc: uncertainty, i: initial.

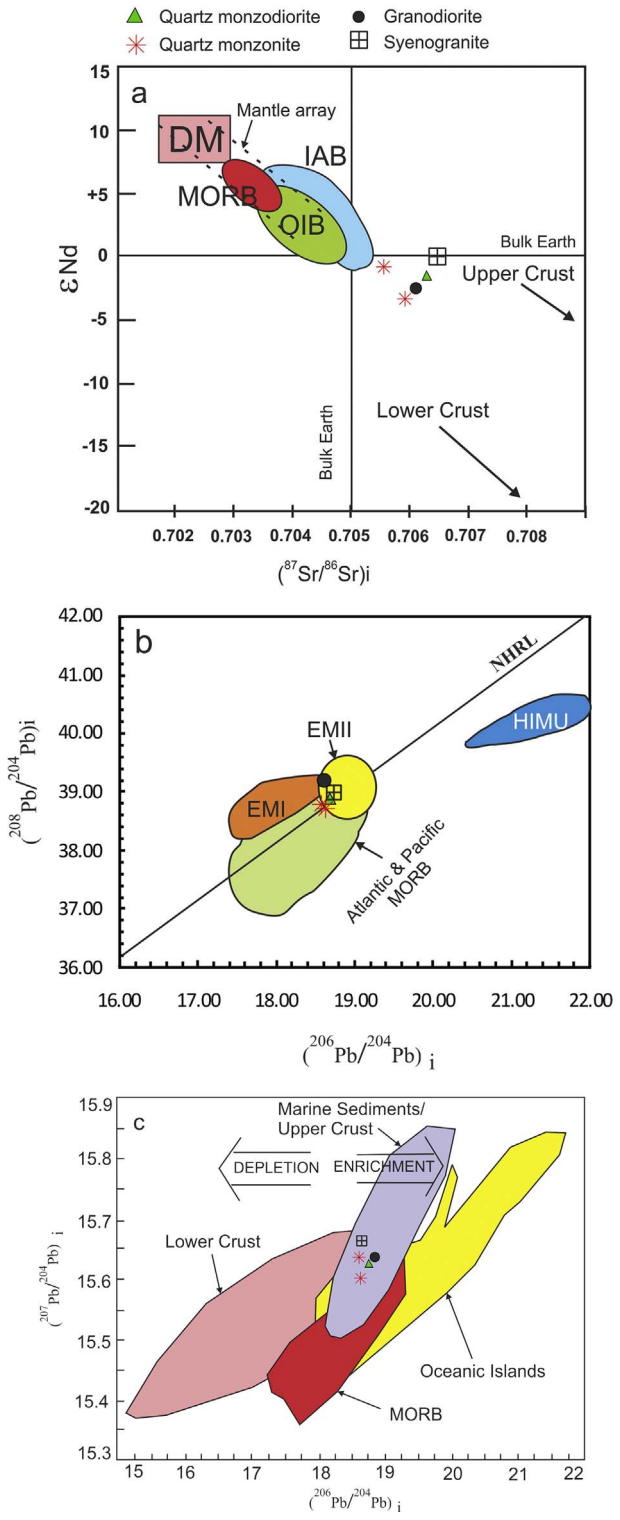

Fig. 14. Plots of Sr–Nd–Pb isotopic compositions for the Kuh-e-Zar intrusive rocks. a) ($^{87}Sr/^{86}Sr$)i versus εNd; b) ($^{208}Pb/^{204}Pb$)i versus ($^{206}Pb/^{204}Pb$)i; c) ($^{207}Pb/^{204}Pb$)i versus ($^{206}Pb/^{204}Pb$)i. MORB: Mid ocean ridge basalts; DM: Depleted mantle; OIB: Ocean-island basalts; IAB: island arc basalts; EM I and II: enriched mantle reservoirs; NHRL: Northern Hemisphere Reference line; HIMU: high U/Pb mantle (e.g., Zindler and Hart, 1986; Rollinson, 1993; Wang et al., 2006).
Initial ratios calculated for 41 Ma. Pb isotope ratios in major terrestrial reservoirs are from White (2003) and references therein.

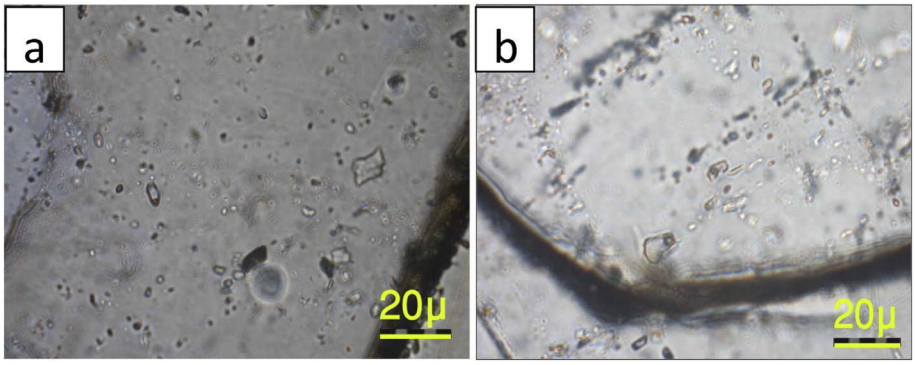

Fig. 15. Micropictures of small size (typically 3–12 μm) liquid-vapor inclusions in the Kuh-e-Zar deposit. The type of inclusions is two-phase, liquid-rich with 5–20% vapor in volume percentage.

slab generates adakites, which are characterized by low Y and Yb_N and high Sr concentrations, high $(La/Yb)_N$ ratios, and LREE enriched rare-earth element patterns (Defant and Drummond, 1990). However, the Kuh-e-Zar intrusive rocks trace element signatures different from those of adakites: they have lower La/Yb ratios and higher Yb concentrations (Fig. 17).

The depth, composition and melting degree of mantle sourced magma can be find out by REEs and their ratios (e.g., La/Yb, La/Sm, Sm/Yb or Dy/Yb) (Aldanmaz et al., 2000; Duggen et al., 2005; Jiang et al., 2009). We performed melting modeling in the Sm/Yb–La/Sm system, which shows that the intrusive rocks were formed by ~1–5% partial melting of garnet-bearing spinel lherzolite (spinel > garnet) (Fig. 18). Thus, based on the isotopic data showing a slightly enriched mantle source, in combination with LREE enrichment and HFSE depletion and the results of melting modeling, we suggest that the parental melts of the Kuh-e-Zar intrusive rocks were derived by the partial melting of subduction-related modified sub-arc mantle. They were likely to have been formed by low-degree melting of a garnet-bearing spinel lherzolite mantle source metasomatized by slab derived fluids. During the migration of melt, additional input of crustal materials could have caused the observed geochemical signatures, especially the isotopic data, of most of the intrusive rocks in the Kuh-e-Zar area.

The U-Pb zircon dating, εNd(t) and $(^{87}Sr/^{86}Sr)i$ values, and geochemical characteristics in Kuh-e-Zar intrusions are very similar to Kashmar granitoids (Shafaii Moghadam et al., 2015) within the center part of the KKBMB and west of the Kuh-e-Zar deposit. The Kashmar granitoids are metaluminous to peraluminous, calc-alkaline and I-type in composition. Similarly, the U-Pb zircon dating of Kashmar granitoids gave ages of 40–41 Ma. They have mostly low whole rock εNd (−0.43 to −2.3) and high $(^{87}Sr/^{86}Sr)i$ (0.705 to 0.707) (Shafaii Moghadam et al., 2015). The intrusion of Kashmar granitoids into volcanic rocks has close relationship to the formation of porphyry Au-, Au–Cu-, and epithermal-type mineralization in the KKBMB.

Thus, we propose that the igneous rocks of KKBMB are products of crustal assimilation by metasomatized mantle wedge melts above the subducting Neotethyan Ocean (Kashmar Neotethyan Ocean) slab beneath SW Eurasia.

9.2. Nature of the ore fluids

Many studies have established the importance of isotopic analyses in elucidating the origin of hydrothermal fluids (Criss and Farquhar, 2008; Huang et al., 2011). The +7.4 to +7.9‰ calculated $\delta^{18}O$ values of the fluid in quartz–specular hematite–gold ± pyrite ± chalcopyrite veinlets strongly support their formation from magmatic waters within the average temperature of 350 °C as obtained from the fluid inclusion studies. Since the gold and sulfide minerals are in general intimately associated with the quartz veinlets at Kuh-e-Zar deposit, it can be further inferred that the ore minerals were also primarily deposited by these fluids. It is crucial to note that the two samples from one mineralized zone might not be representative for the formation of all of the veins in the area, and should not be generalized for the overall history of the fluid evolution at Kuh-e-Zar.

Chalcopyrite ranges in $\delta^{34}S$ values from around −2.4 to +1‰ (average −1.5‰) and the $\delta^{34}S_{H2S}$ in equilibrium with chalcopyrite were estimated to be in the range of −2.5 to +0.9‰ (average −1.5‰). Overall, the sulfides have an isotopic signature around 0‰, consistent with a magmatic source for the sulfur. The composition of this magmatic sulfur may reflect a component derived via leaching of the underlying volcanic rocks or a direct contribution from magmatic fluids.

Fluid inclusions data and mineral assemblages of the Kuh-e-Zar deposit reveal that the ore-forming fluids were a medium-high temperature, medium-low salinity H_2O–NaCl system and a high oxygen fugacity fluid. The homogenization temperature and salinity data indicate the chloride complex was the main ligand for metal transport in

Table 5
Microthermometric data of primary fluid inclusions within quartz of the Kuh-e-Zar deposit.

Sample No.	Vein type	Mineralized zone	T_h (°C)	$T_m$ice (°C)	Salinity (NaCl wt% equiv.)
M4	Qz-SHem-gold	Mohammad Baigi	375–491	−11.5 to −15.7	15.5–19.2
M3	Qz-SHem-gold	Mohammad Baigi	248–330	–	–
2/1-3	Qz-SHem-gold	Mohammad Baigi	385–406	–	–
M20	Qz-SHem-gold	Mohammad Baigi	314–345	−4.1 to −5.3	6.3–8.4
G5	Qz-SHem-gold	Ghar-e-Kaftari	295–336	−9.1 to −11.3	12.9–15.3
SKZ.1	Qz-SHem-gold	Kamar Zard	360–414	−7.7 to −8.8	11.5–12.6
SHA11	Qz-SHem-gold	Shah Ali	287–325	−5.5 to −7.5	8.5–11.1
AMR	Qz-SHem-gold	Amrollahi	419–460	–	–
TRD	Qz-SHem-gold ± Py ± Ccp	Tarik Darreh	338–372	−3.5 to −7.8	5.7–11.5
Z14	Qz-SHem-gold ± Py ± Ccp	Tarik Darreh	271–367	−2.4 to −4.1	4–6.6
JH5	Qz-SHem-gold ± Py ± Ccp	Ghar-e-Saleh	320–384	−4.8 to −6.1	7.6–9.3
A5	Qz-SHem-gold ± Sd	Alireza	320–368	–	–
FR2	Qz-SHem-gold ± Sd	Farshami	328–368	−3.1 to −4.5	5.1–7.2

T_h, homogenization temperature; T_m, temperature for final ice melting. Qz: quartz, SHem: specular hematite, Py: pyrite, Ccp: chalcopyrite, Sd: siderite (Whitney and Evans, 2010).

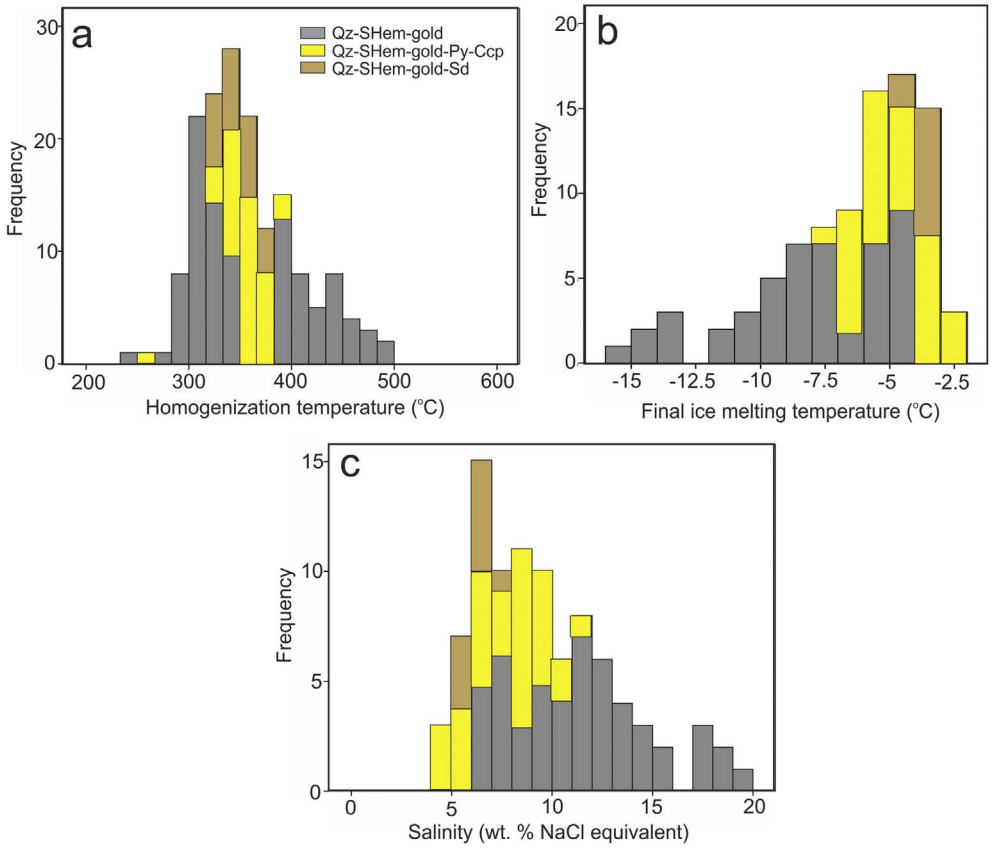

Fig. 16. Histogram showing the thermodynamic data of primary fluid inclusions in the Kuh-e-Zar deposit. a) Homogenization temperature histogram, b) final ice melting temperature histogram, and c) salinity (wt% NaCl equivalent) histogram. (Qz: quartz, SHem: specular hematite, Py: pyrite, Ccp: chalcopyrite, Sd: siderite (Whitney and Evans, 2010).)

Table 6
Stable isotope data from mineralized zones of the Kuh-e-Zar deposit.

Sample location	Host mineral	$\delta^{18}O_{SMOV}$ (‰)	$\delta^{18}O_{water}$ [a] (‰)	$\delta^{34}S_{CDT}$ (‰)	$\delta^{34}S_{water}$ [b] (‰)
Tarik Darreh	Quartz	13.2	7.4		
Tarik Darreh	Quartz	13.7	7.9		
Tarik Darreh	Chalcopyrite	–	–	− 1.1	− 1.2
Tarik Darreh	Chalcopyrite	–	–	− 2.4	− 2.5
Farshami	Chalcopyrite	–	–	+ 1	+ 0.9

[a] Estimated using the equation of Zhang et al. (1989) based on 350 °C.
[b] Estimated using the equation of Li and Liu (2006) based on 350 °C.

hydrothermal solutions (Pirajno, 2009). The pressure determined for Kuh-e-Zar deposit is ca. < 60 MPa, which is equivalent to a depth of approximately < 6 km and < 2.5 km, assuming hydrostatic and lithostatic pressure, respectively (Fig. 19). This implies that the veins were formed at shallow depth.

Homogenization temperature shows a positive correlation with fluid salinity (Fig. 20), similar to the process of fluid mixing (Shepherd et al., 1985; Zhang, 1997). Also, relationship between homogenization temperature, salinity, and fields for various fluid types (Fig. 21) probably indicates that magmatic-meteoric mixing fluid was responsible for ore mineralization at the Kuh-e-Zar. The Figs. 20 and 21 showed a fluid evolution trend shifting from high to relatively low homogenization temperature and salinity. The homogenization temperature and salinity of the quartz–specular hematite–gold veins are higher than both quartz–specular hematite–gold ± pyrite ± chalcopyrite and quartz–-specular hematite–gold ± siderite veins (Figs. 20 and 21). The fluid mixing is well known that this mechanism can play an important role in generation of large hydrothermal ore deposits (Zhu et al., 2001; Cooke and McPhail, 2001; Fan et al., 2011; Gu et al., 2011; Zhai et al., 2013). The homogenization temperature and salinity of ore-fluid are decreased due to mixing of high-temperature and –salinity magmatic water and low-temperature and –salinity meteoric water. The decrease of temperature is one of the most important mechanisms of decrease of solubility chloride complex (Pirajno, 2009) and Au precipitation. However, changing of other factors such as pH and fO_2 is certainly affected.

9.3. Comparison of the Kuh-e-Zar deposit with IOCG deposits

The Kuh-e-Zar deposit shows several signatures similar to those of IOCG deposits, whereas other characteristics are unusual of IOCG deposits. An empiric definition of IOCG deposits is summarized as having the following five characteristics (Williams et al., 2005): (1) copper, with or without gold, as economic metals, (2) hydrothermal ore styles and strong structural controls, (3) abundant magnetite and/or hematite, (4) Fe oxides with Fe/Ti ratios greater than those in most igneous rocks and bulk crust, and (5) no clear spatial associations with igneous intrusions as, for example, displayed by porphyry and skarn ore deposits.

The tectonic setting for the intrusive rocks in the Kuh-e-Zar area is a subduction-related continental arc that is abnormal for IOCG deposits, which are typically found in intra-continental orogenic collapse, intra-continental anorogenic magmatism, and extension along a subduction-

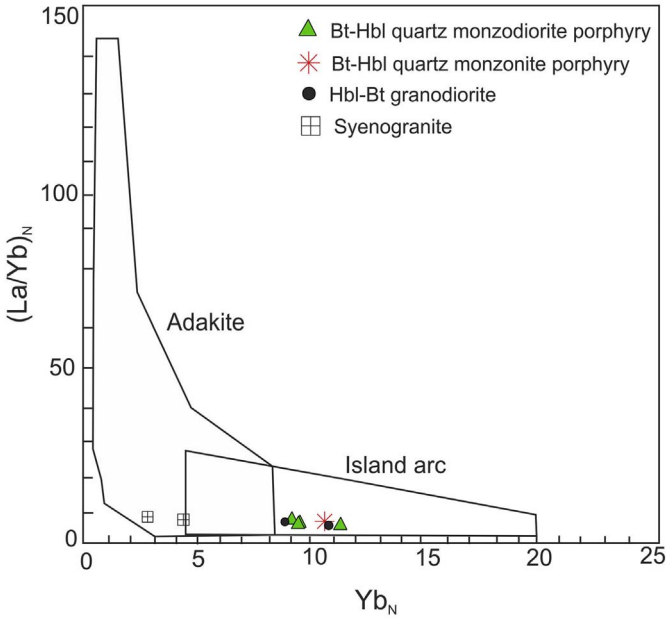

Fig. 17. Plot of Kuh-e-Zar intrusives on Yb_N vs. $(La/Yb)_N$ diagram.
Fields after Li et al. (2009).

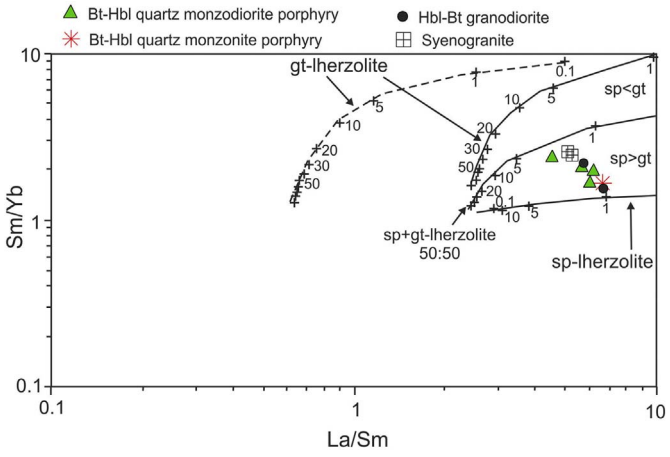

Fig. 18. Plot of Kuh-e-Zar intrusives on Sm/Yb vs. La/Sm diagram for determination of magma source.
(Modified after Aldanmaz et al. (2000).)

related continental margin (Hitzman, 2000; Williams et al., 2005).

According to Pollard (2002), the intrusions associated with IOCG deposits are typically granite, resulting partial melting of middle to lower crusted rocks with a variable mantle input. Sillitoe (2003) proposed a close genetic relationship between IOCG deposits in northern Chile and dioritic plutons. Hitzman et al. (1992), Williams et al. (2005), and Groves et al. (2010) suggested that IOCG deposits have a clear temporal, but not spatial, relationship to major magmatic intrusions. These intrusions are commonly mafic (even ultramafic) to felsic alkaline to sub-alkaline rocks. The Kuh-e-Zar deposit has a genetic relationship to calc-alkaline monzodioritic to granitic intrusions.

The Kuh-e-Zar deposit alteration zones are silicification, propylitic, minor albitization, and sericitic-argillic. Oliver et al. (2004) suggested that mixing of magmatic S-bearing fluids and brines could be formed the albitization in the Cloncurry district. Potassic alteration formed at shallow depth such as in the Candelaria–Punta del Cobre (Sillitoe, 2003) and Olympic Dam deposits (Hitzman et al., 1992) and albitization is not development in lower temperature IOCG deposits. Lack of potassic alteration in the Kuh-e-Zar deposit is atypical of IOCG deposits. The large propylitic alteration zone at the Kuh-e-Zar deposit is similar to that observed at Mantoverde, Peru (Vila et al., 1996) and Mont-del'Aigle, Canada (Simard et al., 2006), which are lower temperature and salinity IOCG deposits. At the Olympic Dam, the intense sericitic alteration has been linked to hydrogen ion production during sulfate reduction (Haynes et al., 1995). However, sericitic alteration in the Kuh-e-Zar deposit is limited to intrusive rocks in some places.

Salinity of fluid inclusions from Olympic Dam is 7–42 wt% NaCl equivalent (Haynes et al., 1995). Salinity of the Kuh-e-Zar deposit is comparable to that of Mont-de-l'Aigle (0–26 wt% NaCl equivalent; Simard et al., 2006) and Candelaria–Punta del Cobre (12–24 wt% NaCl equivalent; Marschick and Fontboté, 1996) deposits. The high salinity fluids in IOCG deposits have a close relationship with the regionally extensive albitization (Pollard, 2001, 2002; Oliver et al., 2004) or mobilized evaporates or brines (Barton and Johnson, 1996). Therefore, Lower salinity or a smaller hydrothermal system in mineralization of the Kuh-e-Zar deposit could explain the limited albitization in the area.

The Kuh-e-Zar deposit $\delta^{34}S$ values range from −2.5 to 0.9‰, similar to Australian and Andean IOCG deposits, which are near 0‰ and indicating a magmatic source of sulfur (Williams and Pollard, 2001; Mark et al., 2002; Sillitoe, 2003; Simard et al., 2006; Benavides et al., 2007). Based on fluid inclusion data, the hydrothermal fluids that formed the Kuh-e-Zar deposit could be the result of mixing of a magmatic fluid with meteoric water. Mixing model is proposed for the Olympic Dam and Candelaria–Punta del Cobre deposits (Haynes et al., 1995; Marschick and Fontboté, 2001).

According to Sillitoe (2003), IOCG deposits are characterized by higher copper grades rather than porphyry copper deposits (mostly > 1%) and wide range of low gold grades. The Teresa del Colmo deposit in Chile has resources of 70 Mt at 0.8% Cu with only small traces of gold (Hopper and Correa, 2000), whereas the Monterrosas deposit in Peru has resources of 1.9 Mt at 1.2% Cu and 6 g/t Au (Injoque, 2002). The average value of gold grade from the Kuh-e-Zar deposit is 3 g/t, whereas copper grade is < 0.5%. “the copper in the IOCG deposits is derived from the source of the brines, and precipitation of the copper was a result of mixing of Cu-bearing brine that is evolved extensively via albitization with sulfur-bearing fluid, or reaction of the brine with sulfur-bearing country rocks” (Oliver et al., 2004). Low salinity ore-fluid and limited albitization in the Kuh-e-Zar deposit could probably explain the lower copper grade, similar to the Mont-de-l'Aigle deposit (Simard et al., 2006) and Candelaria–Punta del Cobre deposit (Marschik et al., 2000). In addition, Zhu (2016) believed that the gold value in IOCG deposits and its controlling factors are unclear. He suggested that for exploration of gold-rich IOCG deposits, at province scale the most important thing is to focus on areas both with gold-enriched host rocks and efficient depositional mechanism (e.g., cooling, fluid–rock interaction and fluid mixing) and at a deposit scale the find of gold-rich deposits should also focus on low-temperature deposits (Zhu, 2016). In the Kuh-e-Zar deposit, the gold content of host rock is unknown. But fluid mixing and cooling are probably the most important factor in deposition of minerals. However, other unclear factors are certainly controlled the distribution of gold.

10. Conclusion

1. The Kuh-e-Zar deposit in the KKBMB, NE Iran, is a structure controlled deposit with strong silicate and prophylitic and minor albite alteration. Minerals of the deposit include specular hematite, gold ± pyrite ± chalcopyrite ± galena, quartz, and siderite and are mainly hosted with the three veins. Based on our paragenesis study, the quartz–specular hematite–gold vein is the initial and main mineralization vein, the quartz–specular hematite–gold ± pyrite ± chalcopyrite vein is the second vein, whereas the quartz–specular hematite–gold ± siderite vein is the lasted vein.
2. The geochemistry and geochronology study on the quartz monzodiorite porphyry, quartz monzonite porphyry and granodiorite

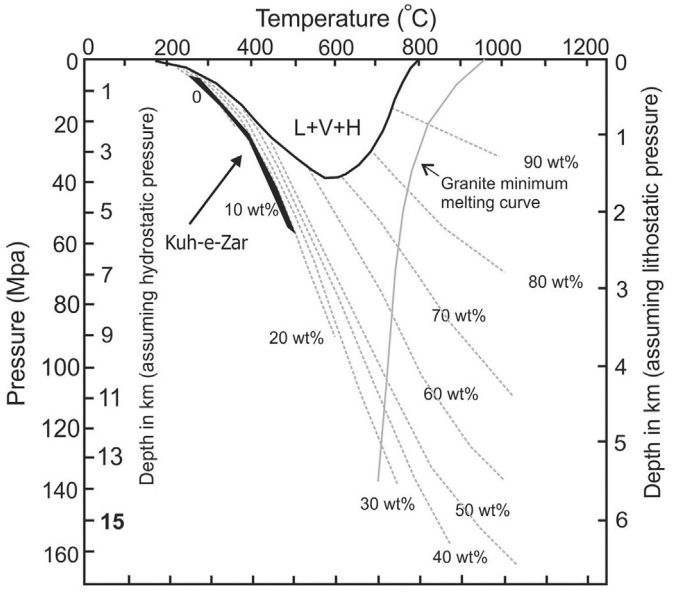

Fig. 19. Pressure-temperature diagram showing phase relationships in the NaCl-H_2O system at lithostatic and hydrostatic pressures (Fournier, 1999). L = liquid, V = vapor, H = halite. Thin dashed lines are contours of constant wt percent NaCl dissolved in brine. Filled gray line indicates granite minimum melting curve. Filled dark line shows the three-phase boundary, L + V + H, for the system NaCl-KCl-H_2O with Na/K in solution fixed by equilibration with albite and K-feldspar at the indicated temperatures. Location of Kuh-e-Zar fluid inclusions data plotted on it.

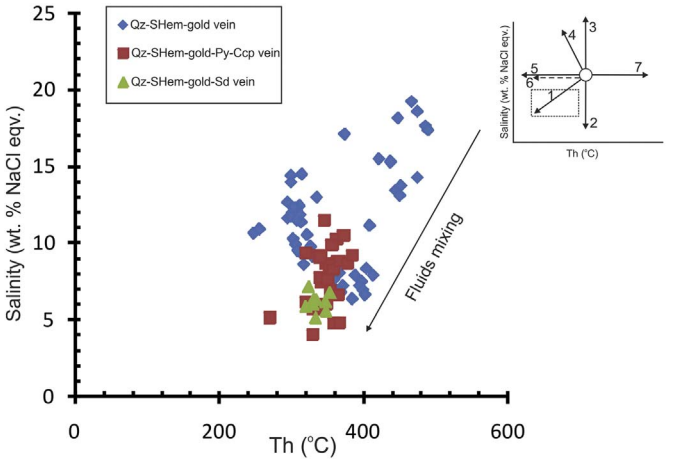

Fig. 20. Homogenization temperature versus salinity of fluid inclusions in the Kuh-e-Zar deposit. Several possible trends of fluid evolution in a temperature-salinity diagram from Shepherd et al. (1985). Trend 1 represents primitive fluid A mixed with cold and low salinity fluid B, trends 2 and 3 represent the result of fluid A isothermally mixing with different salinity fluid B, trend 4 represents the salinity of residual phase increased, caused by boiling of fluid A, trend 5 represents cooling of fluid A, trend 6 represents necking of the fluid inclusion, trend 7 represents leakage of fluid inclusions during heating. (Qz: quartz, SHem: specular hematite, Py: pyrite, Ccp: chalcopyrite, Sd: siderite (Whitney and Evans, 2010).)

indicate that they are products of crustal assimilation by metasomatized mantle wedge melts and were intruded at 40 Ma, in a subduction environment.

3. Fluid inclusion and oxygen and sulfur isotope study indicate that the fluid of the mineralization is magma in origin. The decrease of temperature triggered by fluid mixing of the magmatic and meteoric waters is the dominant mechanism for the precipitation of minerals.
4. Comparison on the characteristics on geology and geochemistry between the Kuh-e-Zar deposit and the typical IOCG deposits suggests the Kuh-e-Zar deposit is a typical IOCG deposit.

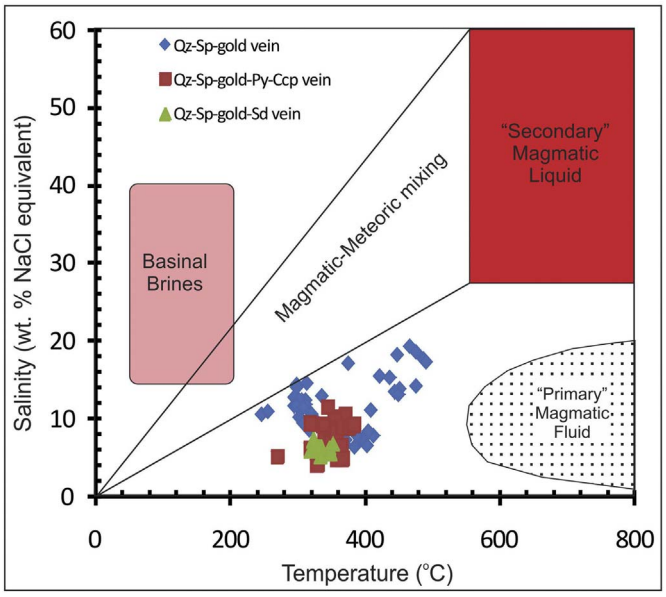

Fig. 21. Homogenization temperature versus salinity diagram for fluid inclusions in the Kuh-e-Zar deposit.
Fields for various fluid types after Beane (1983).

Acknowledgment

The Research Foundation of Ferdowsi University of Mashhad, Iran, supported this study (Project No. 38381.2). We would like to thank Zarmehr Company for the generous support and the access to the mine data. Our thanks are due to Dr. W. Atkinson (University of Colorado) for his constructive comments on the first version of the manuscript, to Dr. T. Vennemann (Institute of Mineralogy and Geochemistry, University of Lausanne, Switzerland) for providing the stable isotope data, and to Dr. G. Gehrels and Dr. V. Valencia (University of Arizona) for the U–Pb zircon dating. Dr. Olof Martinsson is thanked for his comments on preliminary draft of this manuscript. Two anonymous reviewers are thanked for their constructive comments that improved the quality of the final manuscript.

References

Abedi, A., 2003. Mineralogy and geochemical studies in gold mineralized areas at Kuh-e-Zar, Torbat-e-Hydarieh. J. Crystallogr. Mineral. 10 (1), 7–33 (in Persian with English abstract).
Aghanabati, A., 2004. Geology of Iran. Geological Survey of Iran, Tehran, pp. 620.
Aldanmaz, E., Pearce, J.A., Thirlwall, M.F., Mitchell, J.G., 2000. Petrogenetic evolution of late Cenozoic, post-collision volcanism in western Anatolia, Turkey. J. Volcanol. Geotherm. Res. 102, 67–95.
Almasi, A., Karimpour, M.H., Ebrahimi Nasrabadi, Kh., Rahimi, B., KlÖtzli, U., Santos, J.F., 2015. Geology, mineralization, U-Pb dating and Sr-Nd isotope geochemistry of intrusive bodies in northeast of Kashmar. J. Econ. Geol. 1 (7), 69–90 (in Persian with English abstract).
Ansari Jafari, Sh., 2014. Structural Analysis of Zarmehr Gold Ore Deposit. Ferdowsi University of Mashhad, Mashhad, Iran, pp. 166 (unpublished MSC thesis, in Persian with English abstract).
Barton, M.D., 2014. Iron oxide (-Cu–Au–REE–P–Ag–U–Co) systems. In: 2nd edition. Treatise on Geochemistry, vol. 13. pp. 515–541.
Barton, M.D., Johnson, D.A., 1996. Evaporitic-source model for igneous-related Fe oxide–(REE–Cu–Au–U) mineralization. Geology 24, 259–262.
Beane, R.E., 1983. The magmatic–meteoric transition. In: Geothermal Resources Council, Special Report 13, pp. 245–253.
Benavides, J., Kyser, T.K., Clark, A.L., 2007. The Mantoverde iron oxide-copper-gold district, III Región, Chile: the role of regionally derived, nonmagmatic fluids in chalcopyrite mineralization. Econ. Geol. 102, 415–440.
Bodnar, R.J., 1993. Revised equation and table for determining the freezing point depression of H_2O–NaCl solutions. Geochim. Cosmochim. Acta 57, 683–684.
Boynton, W.V., 1985. Cosmochemistry of the rare earth elements, meteorite studies. In: Henderson, P. (Ed.), Rare Earth Element Geochemistry, Developments in Geochemistry 2. Elsevier, Amesterdam, pp. 115–1522.
Chappell, B.W., White, A.J.R., 2001. Two contrasting granite types: 25 years later. Aust. J. Earth Sci. 48, 489–499.

Chen, H., Kyser, T.K., Clark, A.H., 2011. Contrasting fluids and reservoirs in the contiguous Marcona and Mina Justa iron oxide-Cu (-Ag-Au) deposits, south-central Perú. Mineral. Deposita 46, 677–706.
Cherniak, D.J., Watson, E.B., 2000. Pb diffusion in zircon. Chem. Geol. 172, 5–24.
Cooke, D.R., McPhail, D.C., 2001. Epithermal Au–Ag–Te mineralization, Acupan, Baguio district, Philippines: numerical simulations of mineral deposition. Econ. Geol. 96, 109–131.
Criss, R.E., Farquhar, J., 2008. Abundance, notation, and fractionation of light stable isotopes. Rev. Mineral. Geochem. 68, 15–30.
Defant, M.J., Drummond, M.S., 1990. Derivation of some modern arc magmas by melting of young subducted lithosphere. Nature 347, 662–665.
DePaolo, D.J., 1981. Neodymium isotopes in the Colorado Front Range and crustmantle evolution in the Proterozoic. Nature 291, 193–196.
Dickin, A.P., 2005. Radiogenic Isotope Geology. Press Syndicate of the University of Cambridge, London, pp. 175.
Duggen, S., Hoernle, K., Van Den Bogaard, P., Garbe-Schönberg, D., 2005. Post-collisional transition from subduction- to intraplate-type magmatism in the westernmost Mediterranean: evidence for continental-edge delamination of subcontinental lithosphere. J. Petrol. 46, 1155–1201.
Eftekharnejad, J., 1981. Tectonic division of Iran with respect to sedimentary basins. J. Iran. Pet. Soc. 82, 19–28 (in Persian with English abstract).
Fan, H.R., Hu, F.F., Wilde, S.A., Yang, K.F., Jin, C.W., 2011. The Qiyugou gold–bearing breccia pipes, Xiong'ershan region, central China: fluid–inclusion and stable–isotope evidence for an origin from magmatic fluids. Int. Geol. Rev. 53, 25–45.
Farmer, G.L., Barber, D., Andrews, J., 2003. Provenance of Late Quaternary ice-proximal sediments in the North Atlantic: Nd, Sr and Pb isotopic evidence. Earth Planet. Sci. Lett. 209, 227–243.
Fournier, R.O., 1999. Hydrothermal processes related to movement of fluid from plastic into brittle rock in the magmatic-epithermal environment. Econ. Geol. 94, 1193–1212.
Fu, B., Williams, P.J., Oliver, N.H.S., Dong, G., Pollard, P.J., Mark, G., 2003. Fluid mixing versus unmixing as an ore-forming process in the Cloncurry Fe-oxide-Cu-Au district, NW Queensland, Australia: evidence from fluid inclusions. J. Geochem. Explor. 78, 617–622.
Gehrels, G.E., Valencia, V.A., Ruiz, J., 2008. Enhanced precision, accuracy, efficiency, and spatial resolution of U-Pb ages by laser ablation–multicollector–inductively coupled plasma–mass spectrometry. Geochem. Geophys. Geosyst. 9 (3), 1–13.
Gill, J.B., 1981. Orogenic Andesites and Plate Tectonics. Springer, New York.
Girardi, V.A.V., Correa da Costa, P.C., Teixeira, W., 2012. Petrology and Sr–Nd characteristics of the Nova Lacerda dike swarm, SW Amazonian Craton: new insights regarding its subcontinental mantle source and Mesoproterozoic geodynamics. Int. Geol. Rev. 54 (2), 165–182.
Gokce, A., 2000. Ore deposits. In: Cumhuriyet University Publication 100, pp. 450.
Goldstein, S.L., O'Nions, R.K., Hamilton, P.J., 1984. A Sm–Nd isotopic study of atmospheric dusts and particulates from major river systems. Earth Planet. Sci. Lett. 70, 221–236.
Golmohammadi, A., Karimpour, M.H., Malekzadeh Shafaroudi, A., Mazaheri, S.A., 2015. Alteration-mineralization, and radiometric ages of the source pluton at the Sangan iron skarn deposit, northeastern Iran. Ore Geol. Rev. 65, 545–563.
Groves, D.I., Bierlein, F.P., Meinert, L.D., Hitzman, M.W., 2010. Iron oxide copper–gold (IOCG) deposits through Earth history: implications for origin, lithospheric setting, and distinction fromother epigenetic iron oxide deposits. Econ. Geol. 105, 641–654.
Gu, L.X., Wu, C.Z., Zhang, Z.Z., Franco, P., Ni, P., Chen, P.R., Xiao, X.J., 2011. Comparative study of ore-forming fluids of hydrothermal copper-gold deposits in the lower Yangtze River Valley, China. Int. Geol. Rev. 53, 477–498.
Gurabjiripour, A., 2001. Petrology in Kuh-e-Zar Area (Torbat-e-Hydarieh) With Especially Insight on Au Mineralization. Shahid Beheshti University, Tehran, Iran, pp. 126 (unpublished MSC thesis, in Persian with English abstract).
Haynes, D.W., Cross, K.C., Bills, R.T., Reed, M.H., 1995. Olympic Dam ore genesis: a fluid-mixing model. Econ. Geol. 90, 281–307.
Hitzman, M.W., 2000. Iron oxide–Cu–Au deposits: what, where, when and why. In: Porter, T.M. (Ed.), Hydrothermal Iron Oxide Copper–Gold and Related Deposits: A Global Perspective 2. Adelaide, Australian Mineral Foundation, pp. 9–25.
Hitzman, M.W., Oreskes, N., Einaudi, M.T., 1992. Geological characteristics and tectonic setting of Proterozoic iron oxide (Cu–U–Au–REE) deposits. Precambrian Res. 58, 241–287.
Hoefs, J., 1984. Stable Isotope Geochemistry, 3th ed. Springer, Germany.
Hopper, D., Correa, A., 2000. The Panulcillo and Teresa de Colmo copper deposits: two contrasting examples of Fe-ox-Cu-Au mineralisation from the Coastal Cordillera of Chile. In: Porter, T.M. (Ed.), Hydrothermal Iron Oxide Copper-Gold and Related Deposits: A Global Perspective 2. Adelaide, Australian Mineral Foundation, pp. 177–189.
Huang, D.Z., Wang, X.Y., Yang, X.Y., Li, G.M., Huang, S.Q., Liu, Z., Peng, Z.H., Qiu, R.L., 2011. Geochemistry of gold deposits in the Zhangbaling tectonic belt, Anhui province, China. Int. Geol. Rev. 53, 612–634.
Injoque, E.J., 2002. Fe oxide-Cu-Au deposits in Peru: an integrated view. In: Porter, T.M. (Ed.), Hydrothermal Iron Oxide Copper-Gold and Related Deposits: A Global Perspective 2. Adelaide, Australian Mineral Foundation, pp. 97–113.
Jiang, Y.H., Jiang, S.Y., Dai, B.Z., Liao, S.Y., Zhao, K.D., Ling, H.F., 2009. Middle to late Jurassic felsic and mafic magmatism in southern Hunan province, southeast China: implications for a continental arc to rifting. Lithos 107, 185–204.
Karimpour, M.H., 2004. Mineralogy, Alteration, source rock, and tectonic setting of Iron–Oxides Cu–Au deposits and examples of Iran. In: 11th Symposium of Iranian Crystallography and Mineralogy Society, pp. 184–189.
Karimpour, M.H., 2006. Petrology, mineralization and geochemistry of the Sarsefidal prospecting area (Kashmar, Khorasan Razavi). Ahwaz, Iran, Shahid Chamran University, Journal of Science 14, 30–52 (in Persian with English abstract).
Karimpour, M.H., Malekzadeh Shafaroudi, A., 2006. Comparison of the geochemistry of source rocks at Tannurjeh Au-bearing magnetite and Sangan Au-free magnetite deposits, Khorasan Razavi, Iran. Iran. J. Crystallogr. Mineral. 1 (14), 3–26 (in Persian with English abstract).
Karimpour, M.H., Mazloumi Bajestani, A., 1999. Geochemistry, source and potential of gold mineralization in Kuh-e-Zar prospect area, Torbat-e-Hydarieh. J. Geosci. 7 (27–28), 2–13 (in Persian with English abstract).
Kasemann, S., Meixner, A., Rocholl, A., Vennemann, T., Schmitt, A., Wiedenbeck, M., 2001. Boron and oxygen isotope composition of certified reference materials NIST SRM 610/612, and reference materials JB-2G and JR-2G. Geostand. Newslett. 25, 405–416.
Kemp, A.I.S., Hawkesworth, C.J., Foster, G.L., Paterson, B.A., Woodhead, J.D., Hergt, J.M., Gray, C.M., Whitehouse, M.J., 2007. Magmatic and crustal differentiation history of granitic rocks from hafnium and oxygen isotopes in zircon. Science 315, 980–983.
Li, Y., Liu, J., 2006. Calculation of sulfur isotope fractionation in sulfides. Geochim. Cosmochim. Acta 70, 1789–1795.
Li, X.H., Li, W.X., Wang, X.C., Li, Q.L., Liu, Y., Tang, G.Q., 2009. Role of mantle derived magma in genesis of early Yanshanian granites in the Nanling Range, South China: in situ zircon Hf–O isotopic constraints. Sci. China Earth Sci. 39, 872–887.
Mahvashi, M., Malekzadeh Shafaroudi, A., 2016. Cheshmeh Gaz (Nasim) copper deposit, NW Bardaskan: mineralogy, alteration, geochemistry, and determination of model. Iran. J. Crystallogr. Mineral. 3 (24), 419–434 (in Persian with English abstract).
Malekzadeh Shafaroudi, A., Karimpour, M.H., Golmohammadi, A., 2013. Zircon U-Pb geochronology and petrology of intrusive rocks in the C-North and Baghak districts, Sangan iron mine, NE Iran. J. Asia Earth Sci. 64, 256–271.
Maniar, P.D., Piccoli, P.M., 1989. Tectonic discrimination of granitoids. Geol. Soc. Am. Bull. 101, 635–643.
Mark, G., Oliver, N.H.S., Williams, P.J., Valenta, R.K., Crookes, R.A., 2002. The evolution of the Ernest Henry hydrothermal system. In: Porter, T.M. (Ed.), Hydrothermal Iron Oxide Copper–Gold and Related Deposits: A Global Perspective 2. Adelaide, Australian Mineral Foundation, pp. 132–136.
Marschick, R., Fontboté, L., 1996. Copper (–iron) mineralization and superposition of alteration events in the Punta del Cobre belt, Northern Chile. In: Camus, F., Sillitoe, R.H., Peterson, R. (Eds.), Andean Copper Deposits: New Discoveries, Mineralization, Styles and Metallogeny. Society of Economic Geology, Specific Publication 5pp. 171–190.
Marschick, R., Fontboté, L., 2001. The Candelaria–Punta del Cobre iron oxide Cu–Au (–Zn–Ag) deposits, Chile. Econ. Geol. 96, 1799–1826.
Marschik, R., Leveille, R.A., Martin, W., 2000. La Candelaria and the Punta del Cobre district, Chile. Early Cretaceous iron oxide Cu-Au(-Zn-Ag) mineralization. In: Porter, T.M. (Ed.), Hydrothermal Iron Oxide Copper-Gold and Related Deposits: A Global Perspective 2. Adelaide, Australian Mineral Foundation, pp. 163–175.
Mazloumi Bajestani, A., Rasa, 2010. Petrology and alteration of intrusive rocks in Torbat-e-Hydarieh Kuh-e-Zar gold deposit. J. Econ. Geol. 1 (1), 57–69 (in Persian with English abstract).
Mazloumi Bajestani, A., Karimpour, M.H., Rasa, A., Abedini, M., 2007. Application of microthrmometry studies in exploration of Kuh-e-Zar deposit. J. Geosci. 16, 117–130 (in Persian with English abstract).
Middlemost, E.A.K., 1994. Naming materials in the magma/igneous rock system. Earth-Sci. Rev. 37, 215–224.
Ohmoto, H., 1972. Systematics of the sulfur and carbon in hydrothermal ore deposits. Econ. Geol. 67, 551–579.
Ohmoto, H., Goldhaber, M.B., 1997. Sulfur and carbon isotopes. In: Barnes, H.L. (Ed.), Geochemistry of Hydrothermal Ore Deposits. John Wiley and Sons, New York, pp. 517–611.
Oliver, N.H.S., Cleverley, J.S., Mark, G., Pollard, P.J., Fu, B., Marshall, L.J., Rubenach, M.J., Williams, P.J., Baker, T., 2004. Modeling the role of sodic alteration in the genesis of iron–oxide–copper–gold deposits, eastern Mount Isa block, Australia. Econ. Geol. 99, 1145–1176.
Pearce, J.A., 1983. Role of the sub-continental lithosphere in magma genesis at active continental margins. In: Hawkesworth, C.J., Norry, M.J. (Eds.), Continental Basalts and Mantle Xenoliths. Shiva, Nantwich, pp. 230–249.
Pearce, J.A., Cann, J.R., 1993. Tectonic setting of basic volcanic rocks determined using trace element analyses. Earth Planet. Sci. Lett. 19, 290–300.
Pearce, J.A., Harris, N.W., Tindle, A.G., 1984. Trace element discrimination diagrams for the tectonic interpretation of granitic rocks. J. Petrol. 25, 956–983.
Peccerillo, A., Taylor, S.R., 1976. Geochemistry of Eocene calc-alkaline volcanic rocks from the Kastamonu area, Northern Turkey. Contrib. Mineral. Petrol. 58, 63–81.
Pirajno, F., 2009. Hydrothermal Processes and Mineral System. Springer, Australia (1273 pp).
Pollard, P.J., 2001. Sodic (-calcic) alteration in Fe–oxide–Cu–Au districts: an origin via unmixing of magmatic H_2O–CO_2–NaCl ± $CaCl_2$–KCl fluids. Mineral. Deposita 36, 93–100.
Pollard, P.J., 2002. Evidence of a magmatic fluid and metal source for Fe-oxide Cu–Au mineralization. In: Porter, T.M. (Ed.), Hydrothermal Iron Oxide Copper–Gold and Related Deposits: A Global Perspective 1. Australian Mineral Foundation, Adelaide, pp. 27–41.
Pollard, P.J., 2006. An intrusion-related origin for Cu-Au mineralization in iron oxide-copper-gold (IOCG) provinces. Mineral. Deposita 41, 179–187.
Rieger, A.A., Marschik, R., Díaz, M., 2012. The evolution of the hydrothermal IOCG system in the Mantoverde district, northern Chile: new evidence from microthermometry and stable isotope geochemistry. Mineral. Deposita 47, 359–369.
Roedder, E., 1984. Fluid inclusions. In: Ribbe, P.E. (Ed.), Reviews in Mineralogy 12. Mineralogy Society of America (644 pp).

Rollinson, H., 1993. Using Geochemical Data, Evaluation, Presentation, Interpretation. Pearson Education Asia (Pte) Ltd., Singapore.
Rumble, D., Hoering, T.C., 1994. Analysis of oxygen and sulfur isotope ratios in oxide and sulfide minerals by spot heating with a carbon dioxide laser in a fluorine atmosphere. Acc. Chem. Res. 27, 237–241.
Saadat, S., Karimpour, M.H., Ajayebi, K., Stern, C., 2007. Petrology, fluid inclusion thermometry, and geochemistry of Tannurjeh porphyry Cu-Au, northeastern Iran. In: Geological Society of America Abstracts with Programs, vol. 39, no. 6. pp. 412 (abs.).
Sahandi, M.R., Soheily, M., Sadeghi, M., Delavar, S.T., Jafari Rad, A., 2002. Geological Map of Iran, 1:1,000,000. Geological Survey of Iran, Tehran, Iran.
Shafaii Moghadam, H., Li, X.H., Ling, X.X., Santos, J.F., Stern, R.J., Li, Q.L., Ghorbani, G., 2015. Eocene Kashmar granitoids (NE Iran): petrogenetic constraints from U–Pb zircon geochronology and isotope geochemistry. Lithos 216–217, 118–135.
Shahbazian, S.H., 2000. Economic Geology and Exploration of Gold in Kuh-e-Zar Prospect Area. Kharazmi University, Tehran, Iran, pp. 211 (unpublished MSC thesis, in Persian with English abstract).
Sharp, Z.D., 1990. A laser-based microanalytical method for the in determination of oxygen isotope ratios of silicates and oxides. Geochim. Cosmochim. Acta 54, 1353–1357.
Shepherd, T.J., Rankin, A.H., Alderton, D.H.M., 1985. A Practical Guide to Fluid Inclusion Studies. Blackie, London, UK.
Shirzad, B., 2002. Petrology, Geochemistry and Exploration of Gold in Kuh-e-Zar area, Torbat-e-Hydarieh. Ferdowsi University of Mashhad, Mashhad, Iran, pp. 271 (unpublished MSC thesis, in Persian with English abstract).
Sillitoe, R.M., 2003. Iron oxide-copper-gold deposits: an Andean view. Mineral. Deposita 38, 787–812.
Simard, M., Beaudoin, G., Bernard, J., Hupe, A., 2006. Metallogeny of the Mont-de-l'Aigle IOCG deposit, Gaspé Peninsula, Québec, Canada. Mineral. Deposita 41, 607–636.
Sun, S.S., McDonough, W.F., 1989. Chemical and isotopic systematic of oceanic basalts: implication for mantle composition and processes. In: Geological Society of London, Special Publications 42, pp. 313–345.
Tatsumi, Y., Takahashi, T., 2006. Operation of subduction factory and production of andesite. J. Mineral. Petrol. Sci. 101, 145–153.
Vila, T., Lindsay, N., Zamora, R., 1996. Geology of the Manto Verde copper deposit, northern Chile: a specularite-rich hydrothermal tectonic breccia related to the Atacama fault zone. In: Camus, F., Sillitoe, R.H., Petersen, R. (Eds.), Andean Copper Deposits: New Discoveries, Mineralization, Styles and Metallogeny. Society of Economic Geology, Special Publication 5pp. 157–170.
Walker, J.A., Patino, L.C., Carr, M.J., Feigenson, M.D., 2001. Slab control over HFSE depletions in central Nicaragua. Earth Planet. Sci. Lett. 192, 533–543.
Wang, Q., Wyman, D.A., Xu, J.F., Zhao, Z.H., Jian, P., Xiong, X.L., Bao, Z.W., Li, C.F., Bai, Z.H., 2006. Petrogenesis of Cretaceous adakitic and shoshonitic igneous rocks in the Luzong area, Anhui Province (eastern China): implications for geodynamics and Cu-Au mineralization. Lithos 89, 424–446.
White, W.M., 2003. Geochemistry. Cambridge University Press, London.
Whitney, D.L., Evans, B.W., 2010. Abbreviations for names of rock-forming minerals. Am. Mineral. 95, 185–187.
Williams, P.J., 2010. Classifying IOCG deposits. In: Corriveau, L., Mumin, H. (Eds.), Exploring for Iron-oxide Copper Gold Deposits: Canada and Global Analogues. Québec, Geological Association of Canada and Geological Survey of Canada, pp. 11–19.
Williams, P.J., Pollard, P.J., 2001. Australian proterozoic iron oxide- Cu-Au deposits: an overview with new metallogenic and exploration data from the Cloncurry district, Northwest Queensland. Explor. Min. Geol. 10, 191–213.
Williams, P.J., Barton, M.D., Johnson, D.A., Fontboté, L., de Haller, A., Mark, G., Oliver, N.H.S., Marschik, R., 2005. Iron oxide copper-gold deposits: geology, space-time distribution, and possible modes of origin. In: 100th Anniversary of Economic Geology, pp. 371–405.
Wilson, M., 1989. Igneous Petrogenesis: A Global Tectonic Approach. Harper Collins Academic.
www.lab.umcs.lublin.pl/THMS600_linkam.pdf.
Yaghoubpour, A., Shahbazian, Sh., Momenzadeh, M., 1999. Study of gold mineralization in Torbat-e-Hydarieh Kuh-e-Zar. In: 2nd Symposium of Geological Society of Iran, Mashhad, Iran, pp. 564–567.
Yang, J.H., Wu, F.Y., Wilde, S.A., Xie, L.W., Yang, Y.H., Liu, X.M., 2007. Tracing magma mixing in granite genesis, in situ U–Pb dating and Hf-isotope analysis of zircons. Contrib. Mineral. Petrol. 153, 177–190.
Yousefi, L., Karimpour, M.H., Hidarian Shahri, M.R., 2009. Geology, mineralogy, fluid inclusion microthermometry, and ground magnetic survey of magnetite-spcularite-copper-gold mineralization of Shaharak prospect area, Torbat-e-Hydarieh, Iran. J. Crystallogr. Mineral. 16, 505–516 (in Persian with English abstract).
Zarmehr Company, 1999a. Geological Study of Kuh-e-Zar Region. (Mashahd, Iran, 67 pp, in Persian).
Zarmehr Company, 1999b. Exploration of Gold in the Kuh-e-Zar Region. (Mashhad, Iran, 31 pp, in Persian).
Zarmehr Company, 2000. Satellite Image Processing in the Kuh-e-Zar Area. (Mashhad, Iran, 16 pp, in Persian).
Zarmehr Company, 2002. Interpretation of Aeromagnetic Data for Exploration of Gold in the Kuh-e-Zar area. (Mashhad, Iran, 20 pp, in Persian).
Zarmehr Company, 2005a. Detailed Geological Report in Kuh-e-Zar, Mohammad Baigi, and Kamar Zard areas. (Mashhad, Iran, 39 pp, in Persian).
Zarmehr Company, 2005b. Advanced Stage of Exploration in the Kuh-e-Zar deposit. (Mashhad, Iran, 372 pp, in Persian).
Zhai, D.G., Liu, J.J., Wang, J.P., Yao, M.J., Wu, S.H., Fu, C., Liu, Z.J., Wang, S.G., Li, Y.X., 2013. Fluid evolution of the Jiawula Ag-Pb-Zn deposit, Inner Mongolia: mineralogical, fluid inclusion, and stable isotopic evidence. Int. Geol. Rev. 55, 204–224.
Zhang, D.H., 1997. Some new advances in ore forming fluid geochemistry on boiling and mixing of fluids during the processes of hydrothermal deposits. Adv. Earth Science 12, 546–550 (in Chinese with English abstract).
Zhang, L.G., Liu, J.X., Zhou, H.B., Chen, Z.S., 1989. Oxygen isotope fractionation in the quartz-water-salt system. Econ. Geol. 89, 1643–1650.
Zhou, M., Lesher, M.L., Yang, Z., 2004. Geochemistry and petrogenesis of 270 Ma Ni–Cu–(PGE) sulfide-bearing mafic intrusions in Huangshan district, Eastern Xinjiang, Northwest China: implications for the tectonic evolution of the Central Asian orogenic belt. Chem. Geol. 209, 233–257.
Zhu, Z., 2016. Gold in iron oxide copper–gold deposits. Ore Geol. Rev. 72, 37–42.
Zhu, Y.F., Zeng, Y.S., Jiang, N., 2001. Geochemistry of the ore-forming fluids in gold deposits from the Taihang mountains, northern China. Int. Geol. Rev. 43, 457–473.
Zindler, A., Hart, S.R., 1986. Chemical geodynamics. Annu. Rev. Earth Planet. Sci. 14, 493–571.